Debye length and transport properties on composite membranes based on Supported Ionic-Liquid-Like Phases (SILLPs)

Saúl. I. Hernández,[+] Belen Altava,[±] J. A. Portillo-Rodriguez,[++] Iván Santamaría-Holek,[+] C.García-Alcántara,[+] Santiago V. Luis[±], Vicente Compañ[•,*],

[+] Unidad Multidisciplinaria de Docencia e Investigación-Juriquilla, Facultad de Ciencias, Universidad Nacional Autónoma de México (UNAM), Juriquilla, Querétaro, CP 76230, México

[±] Departamento de Química Orgánica, Universitat Jaume I, 12080-Castellón de la Plana, Spain

[++] Facultad de Ingeniería, Universidad Autónoma de Querétaro, Cerro de las Campanas S/N, Centro Universitario, C.P. 76000, Querétaro, México.

• Departamento de Termodinámica Aplicada, Universitat Politècnica de Valencia, C/Camino de Vera s/n, 46022-Valencia, Spain

E-mail: vicommo@ter.upv.es; saul.ivan.hernandez@unam.mx; altava@uji.es; luiss@uji.es; juano_36@hotmail.com; consuelo.garcia@unam.mx;isholek.fc@gmail.com;

Corresponding autor: Vicente Compañ. E-mail: vicommo@ter.upv.es

Authors E-mail: saul.ivan.hernandez@unam.mx; consuelo.garcia@unam.mx; altava@uji.es; luiss@uji.es; isholek.fc@gmail.com; vicommo@ter.upv.es

Abstract

An analysis of the ionic transport properties of BMIM [NTf_2] in Supported Ionic-Liquid-Like Phases (SILLPs)-based membranes has been carried out based on experimental measurements of impedance spectroscopy. The direct current (dc)-conductivity was analyzed in terms of temperature and frequency dependence. The transport quantities such as the conductivity, diffusivity and the density of charge carriers were calculated from a suitable fitting of the loss tangent curves data and the electrode polarization model with the Cole-Cole approximation,. These quantities show a significant improvement in the conductivity, when the ionic liquid is added to the polymeric matrix containing imidazolium fragments. Temperature dependence of

the conductivity is well described by Vogel-Fulcher-Tamman equation. Based on the Eyring's absolute rates theory, the activation entropy and the activation enthalpy also were determined. Our results correlate the Debye length (L_D) with the experimental values of conductivity, electrode polarization relaxation time and sample relaxation time involving. This provide novel aspects on the description of ionic transport in membranes as the diffusivity, mobility and free charge density depend on L_D. Moreover, it was discussed the behavior of the polarization relaxation time, the sample relaxation time and the static permittivity as a function of the temperature.

1. Introduction

Ionic Liquids (ILs) are purely ionic materials with generally low melting temperatures, low vapor pressure, low viscosity, electrochemical stability, and a high conductivity [1]. As a consequence of the uncommon properties displayed by ILs, they have found applications in a wide variety of fields including their use as green solvents in organic synthesis [2], catalysis [3,4], extraction, separation [5], supramolecular chemistry [6,7], as transport agents [8], in pharmaceutical chemistry [9], materials science, or for drug sensing [10], among others. Many of them present high thermal stability, non-volatility, and non-flammability, which along with the mentioned high ionic conductivity allows them to be considered as promising compounds for the preparation of electrochemical devices with a reduction in the potential hazards and environmental impact (i.e. no VOCs generation) [11,12,13,14].

The incorporation of ILs structures into polymeric matrices to form Polymerized Ionic Liquids (PILs) or Supported Ionic Liquids (SILPs or SILLPs) provides an enhancement of those features by integrating the attractive mechanical characteristics of polymers [15,16,17,18]. Supported Ionic-Liquid-Like Phases (SILLPs) can be obtained by covalently bonding ILs-related structural units on the surface of a solid support, allowing the combination of the properties of both components to afford novel advanced materials with important electrochemical applications [19,20]. Both PILs and SILLPs make available interesting advantages when used in electrochemical devices such as dye-sensitized solar cells, lithium batteries, actuators, field-effect transistors, or light emitting electrochemical cells, among others. [11-14,20-21]. Crosslinked macromolecular networks containing IL-like fragments covalently attached

represent a particular kind of conductive SILLPs with remarkable mechanical properties [16,22]. Interestingly, they can be further modified with the use of bulk ILs as porogenic agents in order to obtain composite materials with excellent electrochemical properties in which no appreciable leaching of the IL component is observed [21,23,24]. The balance and interplay between the chemical nature of the cations and anions, the degree of crosslinking, the loading of IL-like fragments in the polymeric matrix and bulk ILs, can be used to fine-tuning the properties and can lead to significant conductivities equivalent to those observed in bulk ILs. Specifically, the crosslinked SILLP containing BMIM [Cl] displayed conductivities of $0.17x10^{-3}$ S/cm at 40 °C, while those with BMIM [NTf_2] presented ionic conductivities of ~10^{-4} S/cm at 40°C, increasing this value one order of magnitude at temperatures close to 100°C [23]. An increase in the amount of bulk IL or a decrease of the crosslinking degree always led to an increase in conductivity [21,23]. It must be noted that for SILLPs the crosslinking can be associated to both the amount of crosslinker used and the presence of strong intra polymeric interactions between the ionic entities. In such cases, the mobility of charge carriers can be related to entropic restrictions, i.e. drastic variations in the number of configurable microstates accessible to them. The influence of these entropic barriers on the conductivity has been discussed in cesium phosphate mixtures that present a superprotonic transition and a symmetry change of their crystal structure [25].

Thus, the use of ILs as conductive fillers to replace phosphoric acid (PA) in composite membranes has been studied to overcome PA disadvantages, such as leaching and conduction instability with time [11,13,26]. In general, IL-based composite membranes reach reasonably high conductivities (>10^{-3} S/cm at 40 °C) when increasing the IL concentration, which enhances the free ionic mobility and the formation of well-developed ionic channels. Thus, for instance, membranes based on fluorine containing polybenzimidazole (PBI) and 1-hexyl-3-methylimidazolium trifluoromethanesulfonate achieved conductivities of 0.016 S/cm at 250 °C under anhydrous conditions [27], while with a protonic IL (1-H-3-methylimidazolium bis(trifluoromethanesulfonyl)imide) reached a proton conductivity of 0.002 S/cm at 190 °C, with the thermal stability in the 150-190 °C range [28]. Proton exchange membranes (PEMs) based on PBI filled with 5 wt. % BMIM bearing different anions (Cl, I, BF_4, PF_6, NCS, Br, NTf_2, BF_4) and under PA doping conditions, exhibited proton conductivities of up to 0.098 S/cm at 120 °C when the BF_4 anion was present [17c-e,18c].

Overall, ionic conductors are key components for many applications, mainly in the field of energy conversion and the development of high-performance ion-conducting solid-state membranes. In this regard, conductivity is a key property to be studied and optimized in those materials. This requires a consistent estimation of the diffusivity (D), the mobility (μ) and ionic carrier density (n).

The present work is aimed to developing a new reliable method to obtain the mobile charge carrier concentration and diffusivity using impedance and dielectric spectroscopic data by modeling the space charge relaxation of a SILLPs sandwiched between two blocking electrodes. The method is primarily based on the models proposed by Schütt [29] and Coelho [30] for ion conducting glasses and generalized by Jönsson et al. [31] In order to verify the applicability of this method, we have used composite polymers doped with variable amounts of 1-butyl-3-methylimidazolium bis(trifluoromethylsulfonyl)imide (BMIM][NTf_2]). Broadband dielectric spectroscopy was employed to investigate the correlation between diffusivity, charge carrier density and Debye length with the structural dynamics of SILLPs. For this purpose, the effect of electrode polarization (EP), previously used and represented by a single Debye relaxation, on the analyses developed by Trukhan [32], Sorensen et al. [33], MacDonald [34],[35], Coelho [36],[37] and Klein et al. [38], has been taken into account to develop a model based on the Cole-Cole relaxation allowing to determine, from experimental data of complex dielectric permittivity, conductivity and loss tangent (tan δ), the diffusivity, the mobility and the mobile ion concentration in SILLPs.

In addition, from the EP approach , represented by a Cole-Cole relaxation model, and the fits of the peaks corresponding to the maximum of the tan δ, we have determined different parameters, such as $M=\Delta\varepsilon_{EP}/\varepsilon_{\infty}$, the electrode polarization relaxation time, $\tau_{EP,}$ and a parameter α which give us the indication of a cumulative process in the system as a consequence of the interactions among charge carriers, which allowed us to calculate, the mobility, the diffusion coefficient, the free charge carrier density as a function of Debye length (L_D), where the characterizing of the ionic transport in the polymeric matrix of a SILLP film present a good correlation with L_D.

2. Experimental details

2.1 Materials

All reagents purchased from commercial suppliers were used without further purification. The imidazolium monomer 1-(4-vinylbenzyl)-3-butyl imidazolium bistriflamide (VBIM [NTf_2], **1**) was synthesized as previously report [39] . 1-Butyl-3-methylimidazolium bis(trifluoromethylsulfonyl)imide (BMIM [NTf_2], **2**) was prepared from commercially available BMIN [Cl] through Cl^- / NTf_2^- exchange using $LiNTf_2$ [40].

SILLPs-based films were prepared (**M1**-**M5**, Scheme 1) by polymerization of mixtures containing an imidazolium monomer (**1**) and an acrylic crosslinking agent (**3**) [23]. Mixtures for **M4** and **M5** films also contained BMIM [NTf_2] (**2**). Table 1 shows the chemical composition of the different SILLPs. Polymerization was carried out using 1% AIBN as the initiator, at 65 ºC, during 24 h, and keeping the monomeric mixture between two glass plates separated by a spacer (0.15 mm). The interaction between the SILLPs and the bulk IL was so effective that no leaching of BMIM [NTf_2] was observed [21,23,24]. The obtained films were fully characterized by FTIR-ATR (MIRacle single-reflection diamond/ZnSe accessory in a Jasco FT-IR 6200 instsrument), Raman spectroscopy (JASCO NRS-3100 dispersive spectrometer with a 785 nm laser, single monochromator, grating 600 lines.mm^{-1}, slit 0.2 mm, resolution 12.75 cm^{-1}, centre wavenumber 1200 cm^{-1}, laser power 90.1 mW, and ten accumulations of 5 s each) and Elemental analysis (LecoTuSpect Micro instrument).

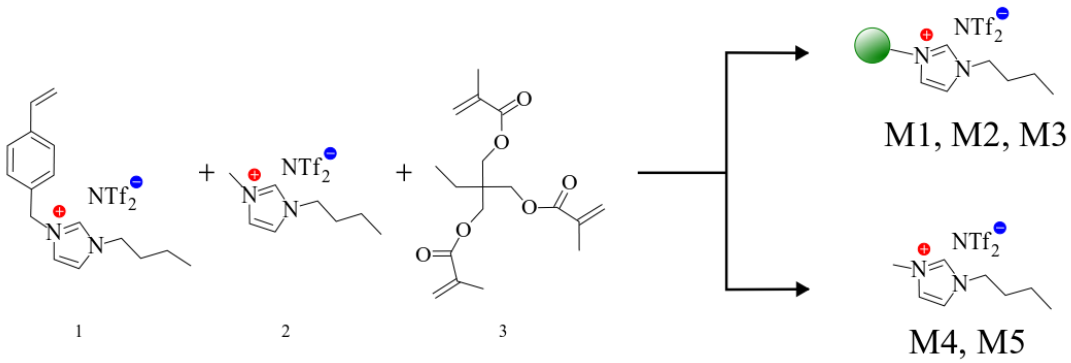

Scheme 1: Synthesis of films **M1**-**M5** (1% AIBN, 65 °C, 24 h)

Table 1: Chemical composition (% wt) of the SILLPs-based films **M1**-**M5** prepared.

SILLP	1	2	3	Thickness (μm)
M1	60%	-	40%	150
M2	70%	-	30%	150
M3	90%	-	10%	150
M4	70%	20%	10%	150
M5	55%	35%	10%	150

2.2. Impedance measurements

The proton conductivity of the films in the transversal direction was measured by impedance spectroscopy at several temperatures in the 0 - 130 ºC range, with 10 ºC steps, in the frequency range of $10^{-1} < f < 10^{7}$ Hz, applying a 0.1 V signal amplitude. A Novocontrol broadband dielectric Spectrometer (Hundsangen, Germany) integrated by an SR 830 lock-in amplifier with an Alpha dielectric interface was used. For that purpose, membranes of 10 mm diameter were sandwiched between two gold circular electrodes coupled to the impedance spectrometer by co-pressing the synthetized materials in a sandwich cell configuration. The measurements have been made following the usual procedures in Electrochemical Impedance Spectroscopy (EIS) [41,42,43]. Before the measurements the sample thickness was measured by a micrometer (results shown in Table 1). The membrane-electrode assembly was annealed in the Novocontrol setup under an inert dry nitrogen atmosphere before starting the measurement. To ensure the measurements reproducibility two temperature cycles were studied. In the first run, the temperature was gradually raised from ambient temperature to 403 K and then lowered to 273 K in steps of 20 K recording the dielectric spectra in each step. In the second cycle of temperature, the dielectric spectra were collected in each step from 273 to 403 K. During the conductivity measurements, the temperature was kept constant at each measuring step using a nitrogen jet (QUATRO from Novocontrol) with a temperature error of 0.1 K, during every single sweep in frequency.

3. Results

3.1. Electrochemical Impedance Spectroscopy

From the dielectric measurements, the dc-conductivity (σ_{dc}) can be obtained using three different procedures. However, all methods are indirect, because they need the criteria to give the value of the dc-conductivity. One of the methods starts from the relationship between the complex dielectric permittivity (ε^*) and the complex conductivity (σ^*) given by $\sigma^*(\omega, T) = j \varepsilon_0 \omega \varepsilon^*(\omega, T)$, where $j = (-1)^{1/2}$ and ε_0 represents the vacuum permittivity and ω the angular frequency of the applied electric field ($\omega = 2 \pi f$). From the dielectric results, the real and imaginary part of the dc-conductivity can be expressed, taking into account the dielectric permittivity $\varepsilon^*(\omega) = \varepsilon'(\omega) - j \varepsilon''(\omega)$, as

$$\sigma'(\omega, T) = \varepsilon_0 \omega \varepsilon''(\omega, T) \quad (1)$$

and

$$\sigma''(\omega, T) = \varepsilon_0 \omega \varepsilon'(\omega, T) \quad (2)$$

Nevertheless, the determination of the real part of the conductivity from the imaginary part of the dielectric permittivity, ($\log \varepsilon'' = \log(\sigma_{dc}/\varepsilon_0) - \log \omega$), where the slope of the $\log \varepsilon''$ versus $\log \omega$ is equal to -1 permits to obtain a good estimation of the dc-conductivity from the intercept of the straight-line at frequency $\omega = 1$, when the Maxwell–Wagner– Sillar (MWS) effects due to the bulk conductivity dominate, as for a pure ohmic conduction [43],[44],[45].

A second approach to obtain the dc-conductivity is the use of the Bode diagram, where the modulus of the complex conductivity $|\sigma^*|$ is plotted versus the frequency ω. As frequency increases, the modulus increases reaching a plateau, while the phase angle $\phi = \tan^{-}(Z''/Z')$ reaches a maximum (or tend to zero). When $|\sigma^*| \rightarrow \sigma_0$ and $\phi = 0$, the ionic conductivity of the sample can be obtained [46].

Finally, another method used frequently to determine the dc-conductivity uses the Nyquist diagrams, where the imaginary part of the impedance is plotted versus the real part of impedance ($-Z''$ vs Z') [47]. Usually, these results are interpreted in terms of the equivalent circuits, which in the case of a homogenous polyelectrolyte comprises a resistance R_0 in series with a circuit made up of an element Rp representing the charge transfer resistance at the

interface sample/electrode in parallel with a capacitor (C). These diagrams are semicircles intersecting the abscissa axis at $Z' = R_0$, because in the intersection with the abscissa axis the imaginary part of the impedance is zero (i.e., the phase angle is zero) and then this value represents the dc-conductivity. On the other hand, it is well-known that polarization relaxation processes in polymers and membranes are not described by a single relaxation time, but by a wide distribution of relaxation times. Therefore, the equivalent circuit should be composed by a resistance R_0, which accounts for the ionic resistance, in series with an assembly of N circuits. Each circuit is made up of a resistance R_i (representing a polarization resistance) in parallel with a constant phase element (CPE) of admittance $Y^* = Y_0(j\ \omega\ \tau\ )^n\ (0 < n \leq 1)$ [48]. This CPE accounts for interfacial phenomena in the membrane electrode interface. This procedure was used in this work, where impedance spectroscopy measurements were carried out for the samples **M1**-**M5** from 20 $°C$ to 130 $°C$ in order to obtain the conductivity in addition to the ionic transport properties of the samples, and Figure 1 shows the different Nyquist diagrams obtained for the five films prepared.

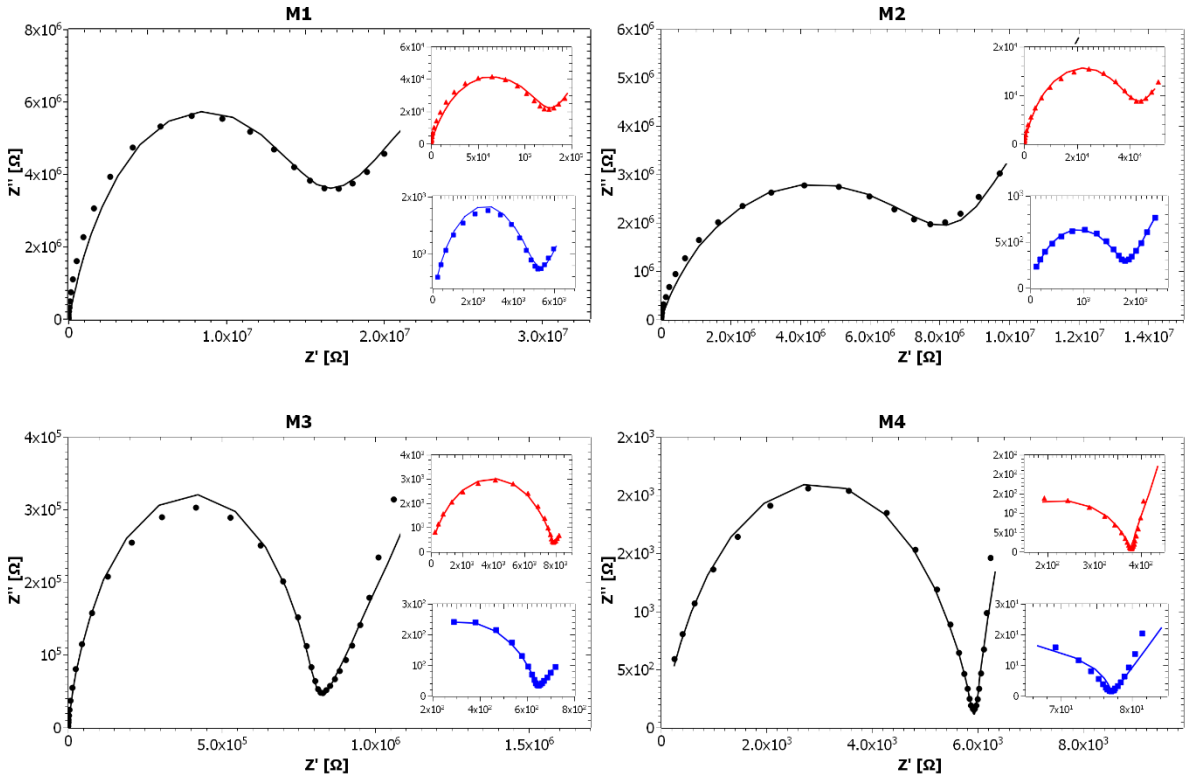

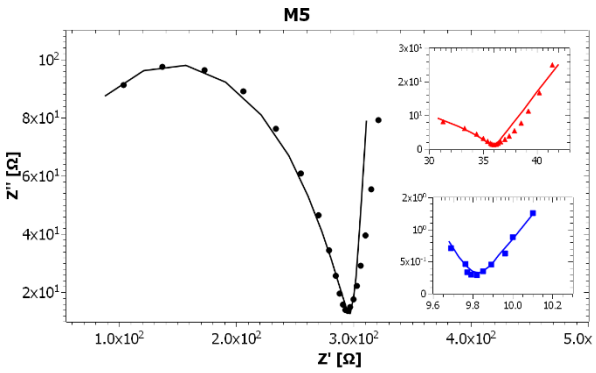

Figure 1. Nyquist diagrams for the samples **M1**-**M5** at 30 ºC. The insets represent the diagrams at 70 and 110 ºC.

As shown in Figure 1, the representation of the imaginary part of the impedance Z" vs. the real part of the impedance Z' in (Ω) displayed the Nyquist plots with semicircles intersecting the abscissa axis at $Z' = R_0$ for all the composite membranes studied. At this point, the imaginary part of the complex impedance is equal to zero (i.e., the phase angle is zero) and then, this value represents the bulk resistance of the composite membrane [49]. The estimated values for the second interception of the ideal semicircle with the x-axes increases with temperature, as typically observed for composite membranes. The figure also shows that for **M1**-**M5** membranes, a spike can be observed in the experimental Nyquist diagrams at all temperatures studied. As inferred from figure 1, the intercept of the semicircles with the x-axes decrease with temperature increase, as typically observed for composite membranes. Experimental departure from semicircles is usually the result of polarization electrode processes and other possible effects taking place at the membrane/electrode interface, leading to the presence of a distribution of relaxation times, instead of a single one [48].

The impedance results for these complex systems, generally have been analysed in terms of equivalent circuits composed of a resistance R_p, representing the charge transfer resistance at the interface sample/electrode, connected in parallel with a constant phase element (CPE), which is equivalent to the sample/electrode double layer (see Figure SI-1 in the Supplementary Information).

The following equation is used to fit experimental data to the theoretical data,

$$Z^*(\omega) = Ro + \sum_i \frac{R_{pi}}{1+(j\omega\tau_i)^{a_i}} \qquad (1)$$

Where $R_{pi}$is a polarization resistance, τ_i *i*s the relaxation time, j = $(-1)^{1/2}$ as mentioned before, and a_i is a parameter $(0 < \alpha < 1)$ which characterizes the distribution of relaxation times yielding a Debye system impedance when $\alpha = 1$. Note that Eq. 1 is equivalent, at the impedance level, to the Cole-Cole complex dielectric constant expression.

In some cases, these systems combine polarization processes with a frequency that is independent of the sample resistance, or ohmic resistance (R_0), and other frequency independent processes. In such a case, the equivalent electrical circuit can be given by a series of Cole-Cole functions in series with R_0. In our case, the impedance of the circuit is modelled by a series combining two Cole-Cole functions to bind the bulk properties and the polarization effects. The bulk resistance, R_0 is determined from the point of intersection of the semicircle at higher frequency (extrapolated end) with the real Z' axis and the corresponding conductivity (σ_{dc}) is calculated by the expression:

$$\sigma' = \sigma_{dc} = \frac{L}{S}\frac{Z'}{\left[(Z')^2 + (Z'')^2\right]} = \frac{L}{S \cdot R_0} \qquad (2)$$

where L is the thickness of the sample, S the effective area of the membrane (given by the area of the electrodes used for the measurement), and Z' and Z" are the real and imaginary part of the complex impedance, respectively.

The values for the impedance of the composite membranes and their conductivity calculated through the fitting of the Nyquist diagrams shown in Figure 1, by using the Eq. (1) with i=2 and applying the Eq. (2) for conductivity. The values of the parameters of Eq.(1) obtained by fit of the experimental data are summarized in Table SI-1 in the Supplementary Information.

Once the dc-conductivity values are obtained from Nyquist diagrams, its behavior with temperature is found. So, we can see in the Figure SI-2 in the Supplementary Information, that the dc-conductivity is in agreement with a Vogel-Fulcher-Tamman (VFT) equation behavior:

$$ln\sigma_{dc} = ln\sigma_{\infty} - \frac{B}{(T-T_0)} \qquad (3)$$

Where B is a fitting parameter related to the curvature of the plot that may be seen as the high temperature activation energy of the process underlying the dc-conductivity, σ_∞ is the pre-factor related to the conductivity limit at high temperatures and T_0 is the Vogel temperature considered as the one at which the relaxation time would diverge. The parameters values obtained from the fitting to Eq.(3) for each temperature are summarized in Table 2. A close inspection of this figure shows that conductivity increases with the amount of free ionic liquid (**M5** > **M4** >> **M3**) and when the amount of crosslinking agent decreases (**M3** > **M2** ≈ **M1**), which is, besides, associated to a higher content in polymer supported imidazolium moieties. It should be noted that the Vogel temperature increases for lower crosslinking degrees (**M3** > **M2** > **M1**), but decreases with the amount of free IL in the composite (**M4** > **M5**). Thus, the observed conductivity follows the order $\sigma(\mathbf{M1}) \approx \sigma(\mathbf{M2}) < \sigma(\mathbf{M3}) < \sigma(\mathbf{M4}) < \sigma(\mathbf{M5})$. For example, at 50 °C the conductivities were 2.3x10^{-6} S/m (**M1**), 2.2x10^{-6} S/m (**M2**), 5.6x10^{-5} S/m (**M3**), 2.1x10^{-4} S/m (**M4**), and 1.2x10^{-2} S/m (**M5**), while at 100 °C were 2.3x10^{-4} S/m (**M1**), 2.4x10^{-4} S/m (**M2**), 2.5x10^{-3} S/m (**M3**), 2.1x10^{-2} S/m (**M4**), and 7.4x10^{-2} S/m (**M5**).

Table 2: Vogel Fulcher-Tamman (VFT) parameters obtained from the fitting of experimental data shown in figure 1 to Eq. (3) for the samples analyzed in this study. The values of χ^2 parameters represent the sum of the square deviations between the experimental data and theoretical values.

Membrane	$ln\sigma_\infty$	B (K)	T_0 (K)	χ^2
M1	9.34	4130	137	0.05
M2	8.02	3510	155	0.04
M3	4.60	1860	193	0.05
M4	2.69	1120	195	0.01
M5	3.09	1210	183	0.01

The calculated activation energy from VFT equation considering all the range of temperatures follows the trend $E_{act}(\mathbf{M1}) = 34.3\ \frac{kJ}{mol} < E_{act}(\mathbf{M2}) = 31.2\ \frac{kJ}{mol} < E_{act}(\mathbf{M3}) = 15.5\ \frac{kJ}{mol} < E_{act}(\mathbf{M4}) = 9.3\frac{kJ}{mol} < E_{act}(\mathbf{M5}) = 8.5\frac{kJ}{mol}$. Again, the lower activation energy for **M3** relative to the films **M2** and **M1** can be correlated with the increase in imidazolium units in the polymeric network and the associated decrease in crosslinking that favors an increased mobility

of the polymeric chains and the ionic fragments. For **M4** and **M5**, having the same crosslinking degree, the activation energy decreases when increasing the amount of BMIM [NTf_2] incorporated. It must be noted that these E_{act} values are of the order, although slightly lower, of that on related composite materials like a film similar to **M5** (12.2 kJ/mol)[23]or a PBI membrane containing a 5% of BMIM [NTf_2] (10.9 kJ/mol)[42]. These results suggest that the anionic conduction in these films can occurs following two mechanisms, the hopping between the imidazolium units and a vehicle-type mechanism. The low activation energies displayed by the polymeric imidazolium networks containing additional BMIM [NTf_2] are very attractive for their application in polymer electrolyte membranes in energy applications, as the transport mechanism is less energy demanding.

On the other hand, the temperature dependence of conductivity can be analyzed in terms of the Eyring's absolute rates theory as

$$\sigma(T) \approx C \cdot T \cdot exp\left(-\frac{\Delta G^{**}}{RT}\right) = C \cdot T \cdot exp\left(\frac{\Delta S^{**}}{R} - \frac{\Delta H^{**}}{RT}\right) \quad (4)$$

Eq. (4) constitutes an Arrhenius law in which $\Delta G^{**} = \Delta H^{**} - T\,\Delta S^{**}$ has been considered. *C* is a pre-factor that only depends of the frequency, ΔG^{**} is the activation Gibbs free energy of the microscopic charge conduction process in the sample, ΔS^{**} is related with the thermodynamic activation of entropy associated with the macroscopic structural changes of the material that give rise to entropic restrictions during the motion of the charges carrier, ΔH^{**} is the enthalpy change associated to the conduction process, T is the absolute temperature and R the gas constant. Since the charge transport is thermally activated, the energy ΔG^{**} involves the formation of the activated complex linked to ion hopping. The values of ΔH^{**} and ΔS^{**} can be obtained from the slope and the T-intercept of the plot $\ln(\sigma/T)$ vs. 1000/T, respectively, see Figure 2.

The Table 3 shows the values of $\mathbf{\Delta H^{**}}$and $\mathbf{\Delta S^{**}}$ associated with the conductivity calculated through Eq. (4).

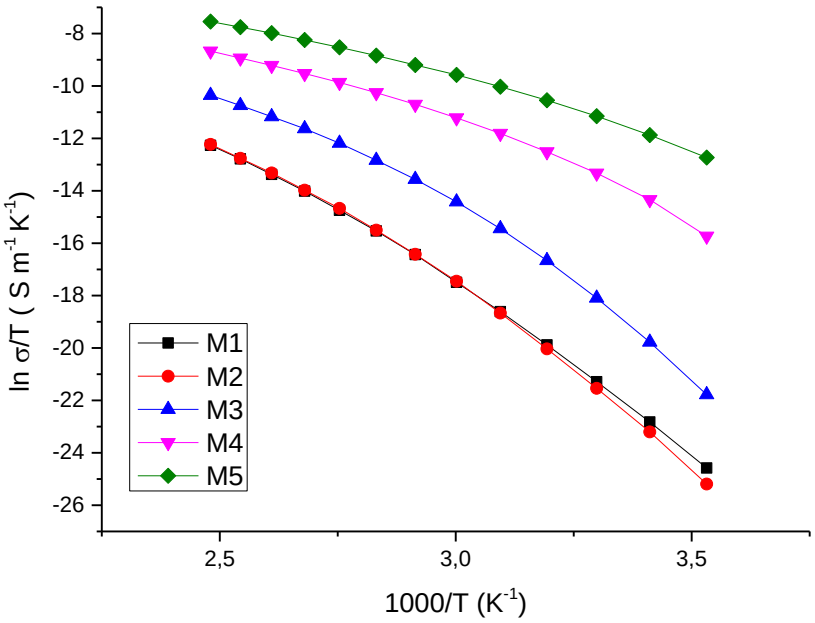

Figure 2: Temperature dependence of ln(σ/T) for the different composite membranes.

Table 3: Values of activation enthalpy (ΔH^{**}), entropy (ΔS^{**}) and activation energy (E_{act}) for all samples studied.

Sample	**E_{act} kJ mol^{-1}**	**ΔH^{**} kJ mol^{-1}**	**ΔS^{**} J mol^{-1} K^{-1}**
M1	34.3±2.8	72.4±1.0	46.2±2.4
M2	29.2±2.3	69.6±1.3	39.6±3.2
M3	15.5±1.4	54.9±1.1	13.8±2.8
M4	9.3±1.1	37.8±0.8	-16.9±2.1
M5	8.5±0.6	31.5±0.7	-17.6±1.8

It can be observed that, for all samples, ΔH^{**} and ΔS^{**} decrease with the loading of IL-like fragments covalently attached to the polymeric matrix, decreasing additionally for **M4** and **M5** in the presence of the bulk IL. For the non-doped membranes, the decrease in activation entropy, from **M1** to **M2** and from **M2** to **M3**, is significantly more important that the one in activation enthalpy. Changes in both ΔH^{**} and ΔS^{**} are more abrupt when comparing **M2** and **M3**. This agrees well with the increase in the density of covalently attached imidazolium units and the simultaneous decrease in crosslinking favoring intrapolymeric coulombic and hydrogen bond

interactions, which is very relevant in particular for **M3** (10% of crosslinker and 90% of polymeric benzyl butyl imidazolium units). Abrupt changes in ΔH^{**} and ΔS^{**} are also observed when comparing **M3** and the films doped with BMIM [NTf_2], displaying identical crosslinking values and similar loadings of imidazolium units (supported IL-like units plus bulk IL units), while a minor decrease in both values is observed when the amount of bulk IL is increased in **M5**. More relevantly, ΔS^{**} becomes negative for the two films doped with BMIM [NTf_2] being more negative for the polymer containing a higher amount of this IL. Such a change could be related with a decrease in the free volume of these systems as the amount of free IL increases and associated to strong supported IL unit-bulk IL unit-supported IL unit interactions.

A representative dielectric spectrum of all the samples (**M1**-**M5**) at 60ºC and 110ºC, is shown in Figure 3, where $\varepsilon', \varepsilon'', \sigma', \sigma''$ and $\tan\delta$, are plotted as a function of frequency. At lower frequencies, the real part of the permittivity is essentially independent of the frequency while the imaginary part increases with decreasing frequency ($\varepsilon'' \approx f^{-1}$). Such behavior represents the direct current conduction. From moderate to low frequencies, the complex permittivity shows a Debye peak or shoulder related with the electrode polarization effect. On the other hand, at the frequency region where the real part of the permittivity starts to decrease almost linearly with the frequency with slope ≈ -1, the imaginary part of the conductivity reaches a maximum, defining then a minimum at higher frequencies, while the real part of the conductivity becomes practically constant, independent of the frequency. At the frequencies at which σ'' reaches the abovementioned minimum, the loss tan δ reaches a maximum, which f_{max} is considered as the frequency where the real part of the conductivity can be considered as the sample conductivity (σ_{dc}).

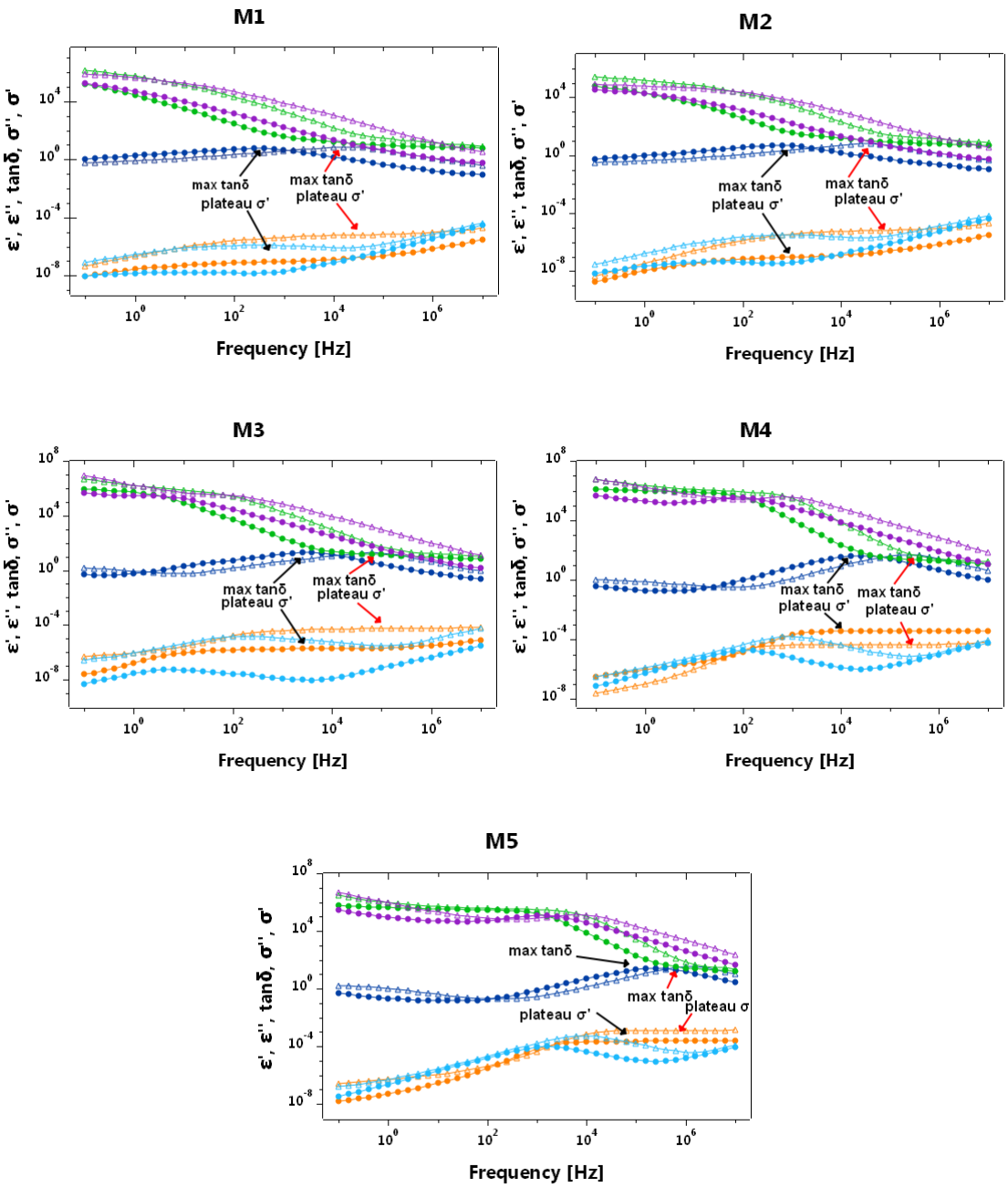

Figure 3: Representation of the real and imaginary parts of permittivity (ε' and ε'') and conductivity (σ' and σ''), and of $tan\delta$ vs. frequency at 60 ºC and 110 ºC.

The Cole-Cole model allows representing the dependence of the complex dielectric permittivity on frequency. In this work we assume that the contribution of the conductivity at low frequencies is generally due to impurities and it can be omitted. Secondly, when the

Maxwell–Wagner–Sillars (MWS) conditions are accomplished (i.e., when the bulk conductivity dominates as for a pure ohmic conduction at high frequencies), then $\varepsilon''(\omega,T) = \sigma_{dc}(\omega,T)/\varepsilon_0\omega$, and the loss tangent, $\tan = \varepsilon'' / \varepsilon'$, can be expressed as follows [25,42,50]

$$\tan\delta = \frac{(\omega\tau_{EP})^{\alpha} sin\left(\frac{\pi\alpha}{2}\right)}{1+(\omega\tau_{EP})^{\alpha} cos\left(\frac{\pi\alpha}{2}\right)+\frac{(\omega\tau_{EP})^{2\alpha}}{M}} \quad (5)$$

With $M=\Delta\varepsilon_{EP}/\varepsilon_{\infty}$, τ_{EP} being the electrode polarization relaxation time and α an exponent being the indication of a cumulative process in the system as a consequence of the interactions among charge carriers. If $\alpha=1$, then Eq. (5) is reduced to the Coelho model, where the EP behavior is represented by a single Debye relaxation.

Figure 4 shows the values of tan δ as a function of the frequency for all the samples studied at different temperatures. As shown, a maximum in the curves is observed at each temperature, which is associated to the plateau of the real part of the conductivity observed in the Bode diagrams (see Figure SI-2 in the Supporting Information). This maximum always shifts to higher frequencies and increases in intensity as a function of temperature. Some differences, however, are observed for the different membranes. How we can see for the samples M4 and M5, the increase in the temperature produces a growth in maximum intensity respect the samples M1 and M2 where they are not free IL embedded and practically the same amount of porogenic agent (VBIM [NTf2]) bulk IL.

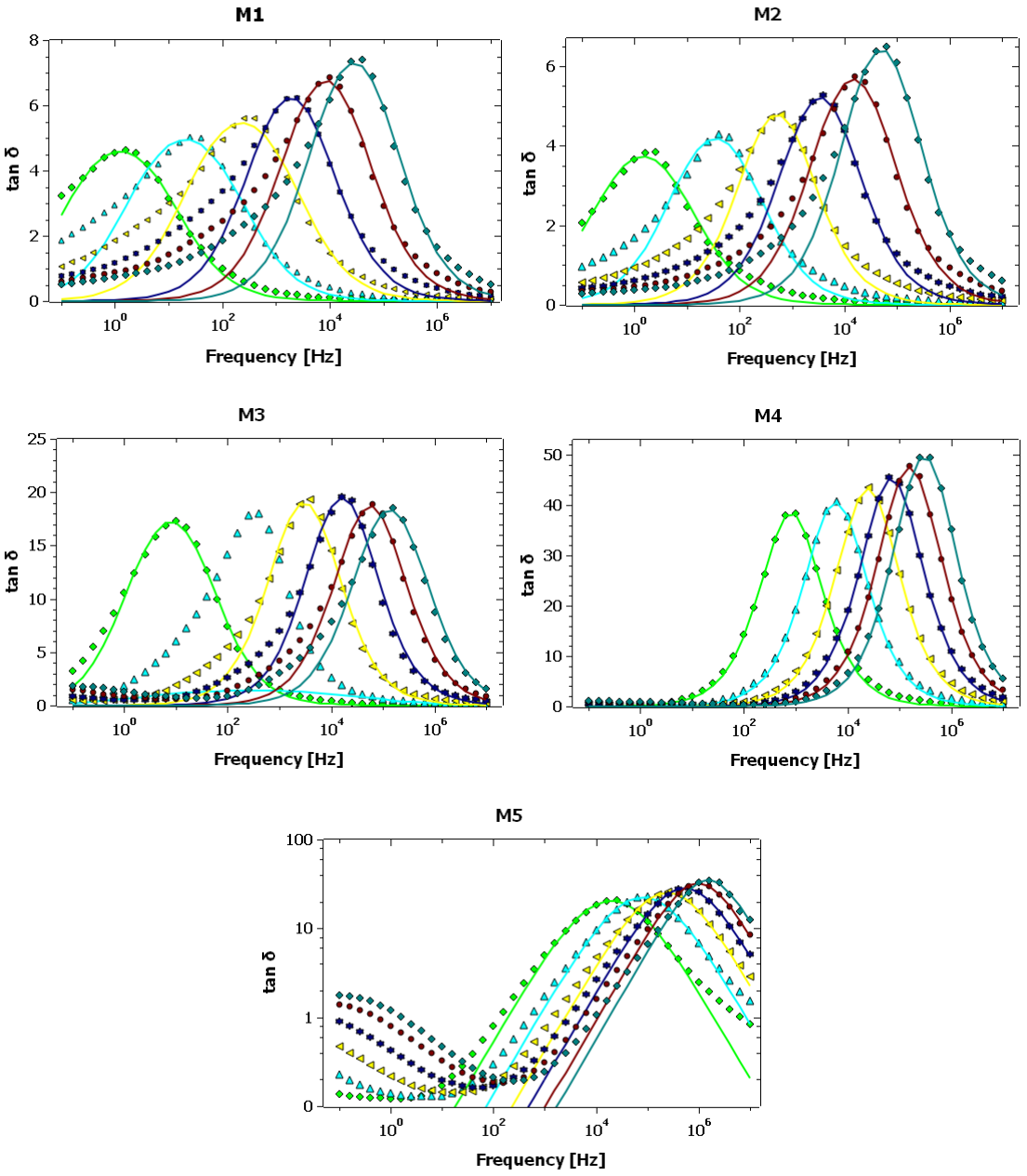

Figure 4: Tan δ as a function of the frequency for all the membranes (◆ 20°C, ▲ 40°C, ◀ 60°C, * 80°C, ● 100°C, ◆ 120°C). The fitting of Eq. (5) is showed as a continuous line for each temperature.

Equation 5 was used to fit the experimental data shown in Figure 4 in order to provide an estimation of the parameters M, τ_{EP} and α. The values of these parameters are given in Table SI-2 in the Supplementary Information, for the temperatures 20, 40, 60, 80, 100 and 120 ºC. The standard deviation of M, τ_{EP} and α parameters determined from the fitting curves remained less than 5%. It is worth mentioning that $\alpha \leq 1$, meaning that interactions between charge carriers are present but they are not dominant for the transport process. The values of the relaxation time τ_{EP}, the parameter M and α, showed clearly a dependence on the temperature. While M does not seem to have a clear dependence on temperature, however the relaxation time (τ_{EP}) and α increases with the temperature for all the membranes, being the values for the electrode polarization time significantly lower for the membranes containing the adsorbed bulk IL BMIM [NTf_2] (**M4**, **M5**).

4. Mobility, diffusivity and free charge density

The mobility and free charge density can be obtained from the measurements of loss tangent. Considering that the anion and cation have the same mobility, μ, and neglecting the ion-ion interaction, the dc-conductivity is given by

$$\sigma_{dc} = nq\mu \qquad (6)$$

where μ is the mobility, q the charge of a monovalent anion and n is the equilibrium number density of free negative charges, i.e. the total anion concentration in the sample. Equation (6) assumes that the anion transfer number is equal to one, being only applicable in the case of cations that are practically immobile. This approximation is plausible taking into account that imidazolium cations derived from the monomer **1** are covalently linked to the polymeric chains and if we accept a reduced mobility for the imidazolium cation in BMIM [NTf_2] as a consequence of its larger size in comparison with that of the counteranion. Therefore, the mobility will be restricted to the anions until the system reach the equilibrium, where the concentration of anions (NTf_2^-), will be constant in space and time. In such a situation, the Debye length, L_D, which is a measure of the length scale of the electrostatic double layer, is written as

$$L_D = \left[\frac{\varepsilon_\infty \, \varepsilon_{vac} \, k \, T}{q^2 \cdot n}\right]^{1/2} \quad (7)$$

Being k the Boltzmann's constant, ε_∞ the dielectric constant at high frequencies, ε_0 the vacuum permittivity, q is the charge of a monovalent anion, n the equilibrium concentration of mobile charge and T the temperature.

Taking into account that the maximum in tan δ, following the Cole-Cole model, is verified for [24]

$$\omega_{\max}^{\tan\delta} = \frac{M^{\frac{1}{2\alpha}}}{\tau_{EP}} = \frac{1}{\tau_m} \quad (8)$$

where the relaxation time obtained as $\tau_m = \frac{1}{2\pi f_{max}^{\tan\delta}}$ represents a time constant, which is related with the electrode polarization time relaxation τ_{EP} and the sample relaxation time τ, defined by $\tau = \frac{\varepsilon}{\sigma_{dc}}$, by mean of $\tau_m^2 = \tau \cdot \tau_{EP}$ [25,38,42,50]. Furthermore, the parameter $M=\Delta\varepsilon_{EP}/\varepsilon_\infty$, also defined as $M(L_D) = \frac{L}{2L_D}$ [38], can be expressed for a Cole-Cole model as

$$M = \left[\frac{\tau_{EP}}{\tau}\right]^{\alpha} \quad (9)$$

where τ is the sample relaxation time written as

$$\tau = \frac{\varepsilon}{\sigma_{dc}} = \frac{\varepsilon_\infty \cdot \varepsilon_{vac}}{q \cdot n \cdot \mu} \quad (10)$$

Being ε the dielectric constant of the sample and σ_{dc} its dc-conductivity.

Then, the time τ_{EP} can be expressed as

$$\tau_{EP}(L_D) = \frac{\varepsilon_\infty \, \varepsilon_{vac}}{\sigma_{dc}} [M(L_D)]^{\frac{1}{\alpha}} \quad (11)$$

and the mobility as

$$\mu(L_D) = [M(L_D)]^{\frac{1}{\alpha}} \frac{\varepsilon_\infty \, \varepsilon_{vac}}{n \, q \, \tau_{EP}} \quad (12)$$

Using the eq. (6) the conductivity also can be given in terms of Debye length and polarization relaxation time,τ_{EP}, as

$$\sigma = \frac{\varepsilon_\infty \varepsilon_{vac}}{\tau_{EP}(L_D)} [M(L_D)]^{\frac{1}{\alpha}} \quad (13)$$

Finally, the anion diffusivity can be calculated from the mobility considering the Nernst-Einstein relation,

$$D(L_D) = \frac{M^{\frac{1}{\alpha}} \cdot L_D^2}{\tau_{EP}} \quad (14)$$

The Eq.(14) could also be expressed in terms of the sample relaxation time τ as

$$D(L_D) = \frac{L_D^2}{\tau} \quad (15)$$

and in function of the time relaxation associated to the start of electrode polarization process, τ_m, as

$$D(L_D) = \frac{L_D^2}{\tau_m} M^{\frac{1}{2\alpha}} \quad (16)$$

The free anion charge density is given from diffusivity and conductivity as

$$n(L_D) = \frac{\sigma}{q\ \mu(L_D)} = \frac{\sigma \cdot kT}{q^2\ D(L_D)} \quad (17)$$

and in terms of Debye length, conductivity and sample time relaxation by

$$n(L_D) = \frac{\sigma \cdot kT}{q^2\ D(L_D)} = \frac{\sigma \cdot kT \cdot \tau}{q^2 \cdot L_D^2} \quad (18)$$

From loss tan δ, the parameters M, α and τ_{EP} are obtained, and considering Eq. (15) we also can obtain the constant time, τ_m. Taking into account that $\tau_m^2 = \tau \cdot \tau_{EP}$ [25,38,42,50], the sample relaxation time (τ) can estimated. The Figure 5 (top) shows their dependence with the reciprocal of the temperature. This figure reveals that τ, in general, exhibits a behavior that cannot be described through a simple Arrhenius behavior. This clearly indicates that in the composite membranes **M1**-**M5** a simple dependence with the temperature is not present, for the range of temperatures analyzed, though a decrease with temperature increase is seen for all the samples. A similar situation is present for τ_{EP} (see Figure 5, bottom). Knowing that electrode polarization relaxation time represents the mean time for an ion to travel from one electrode to another, at times longer than τ_{EP}, a large quantity of mobile anions will have built up at the

electrodes, and the dependence with temperature of anion mobility will not present an Arrhenius behavior.

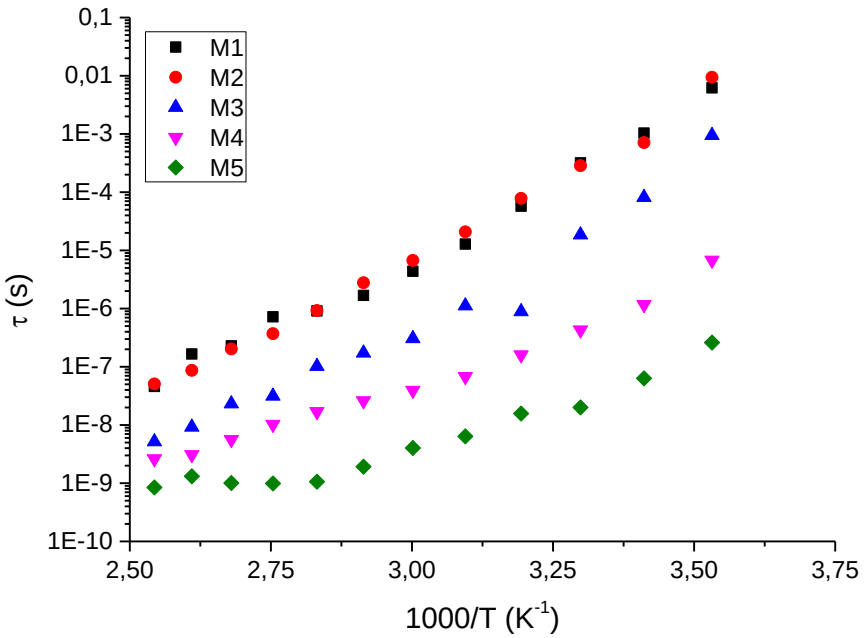

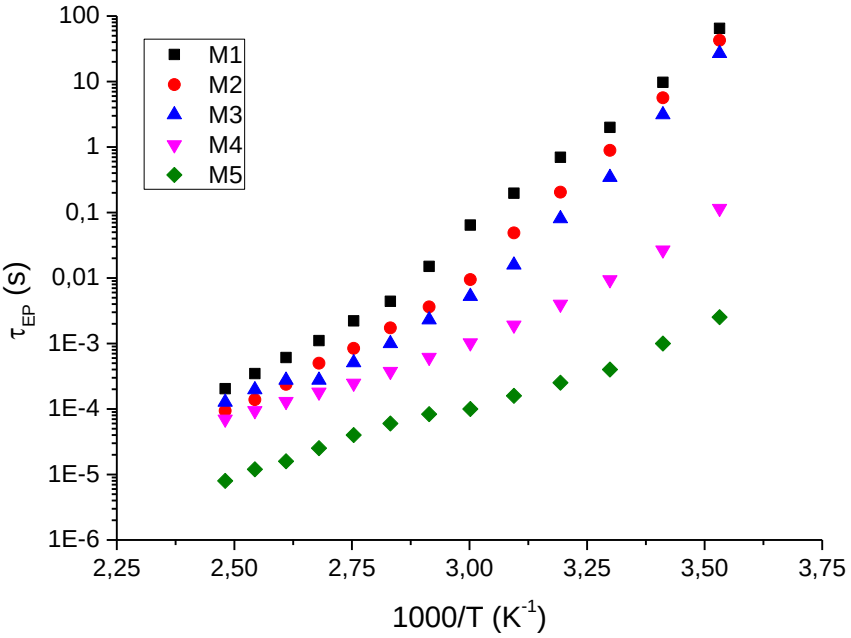

Figure 5: Variation of electrode polarization relaxation time (bottom) and sample relaxation time (top) versus the reciprocal of temperature for the studied samples.

It can also be seen that the relaxation times are relatively similar for **M1** and **M2** (in particular the sample relaxation time) while decrease significantly for **M3**-**M5** displaying higher loadings of imidazolium fragments. The effect is more relevant for the two films containing the BMIM [NTf_2] non-attached covalently to the polymeric matrix (**M4**-**M5**). The composite membrane **M5** containing a larger loading (35%) of free IL than **M4** (20%), but the same total loading of imidazolium units (90%), shows the lower relaxation times. This suggests that the counteranion of the free IL affects the frequency at which the polarization starts to be present and could generate a variation in the length of Debye with the temperature. It is possibly due to the influence of the Debye length thickness have until the system reached the equilibrium.

The diffusion coefficients can be calculated by means of Eqs. (14-16) from the values of M, α, τ_m , τ and L_D. As we have mentioned before, the parameters M and α are obtained from the fitting of the tan δ data using the Eq. (5) (Table SI-2 in the Supplementary Information), while the value of the Debye length can be estimated from M and the sample thickness L. Figure 6 shows the diffusion coefficients for **M1**-**M5** at the temperatures studied. These values are reasonably similar to those for other related systems [51],[52] and indicate that an excellent ion mobility's can be obtained for these films.

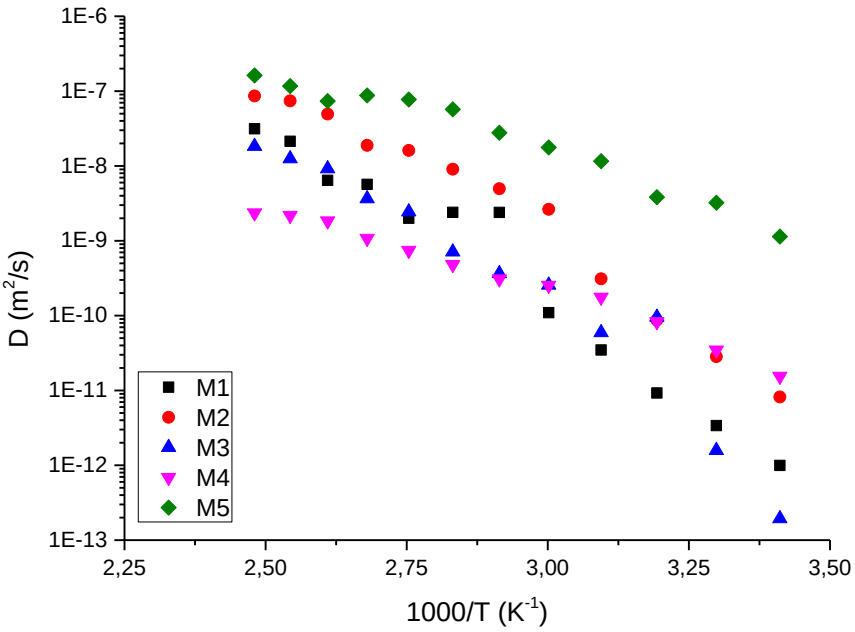

Figure 6: Temperature dependence of the free ion diffusion coefficient D for films **M1**-**M5**. In this figure the diffusion coefficients were calculated from Eq. (15), $D(L_D) = \frac{L_D^2}{\tau}$, using the values of *the* Debye length from the expression $L_D = \frac{L}{2M}$.

The calculated anion diffusivity increased with temperature for all the films. At low temperatures, the trend observed was D(**M5**) > D(**M4**) ≥ D(**M2**) > D(**M3**) > D(**M1**). This behavior agrees reasonably well with the one for the activation energies associated to the diffusivity obtained through the VFT fit where E_{act}(**M5**) < E_{act}(**M4**) < E_{act}(**M2**) < E_{act}(**M3**) < E_{act}(**M1**) and with the values found for the conductivities and their behavior. Some changes are observed at higher temperatures as is reasonable for the increased diffusion coefficient of the polymeric chains bearing imidazolium units. On the other hand, these results are in agreement with the variations of the free charge density of the films, where the average loading of imidazolium units in the polymer, change from $10^{25.2}$ for **M3** until $10^{20.8}$ m^{-3} in the case of **M2**. As expected, the diffusivity varies with reciprocal of the anionic charge density of BMIM-NTf2 for all the SILLPs.

The values for the free anion charge density obtained following Eq. (17) are gathered in Figure 7. Anion charge density is essentially independent of temperature and is directly related with

the loading of imidazolium units in the polymer, following the order n(**M4**) =4x10^{25} m^{-3}> n(**M5**) =3x10^{23} m^{-3}> n(**M3**) =2x10^{23} m^{-3}> n(**M1**) = 10^{22} m^{-3} > n(**M2**) = 3x10^{21} m^{-3}, respectively, where its anion charge density practically is constant with temperature. This pattern is specific of these films based on SILLPs, very different, for instance, of the one found with mixed matrix membrane (MMM) fillers. Thus, in the case of hexacyanocobaltate fillers with formula $M_3[Co(CN)_6]_2 \cdot xH_2O$ (where M = Ni, Co, Fe, Mn and Cd), providing excellent conductivity and diffusivity when the medium contains a sufficient amount of ionic components. Both the L_D and the charge density experience abrupt changes with temperature, depending significantly on the involved transition metal [50].

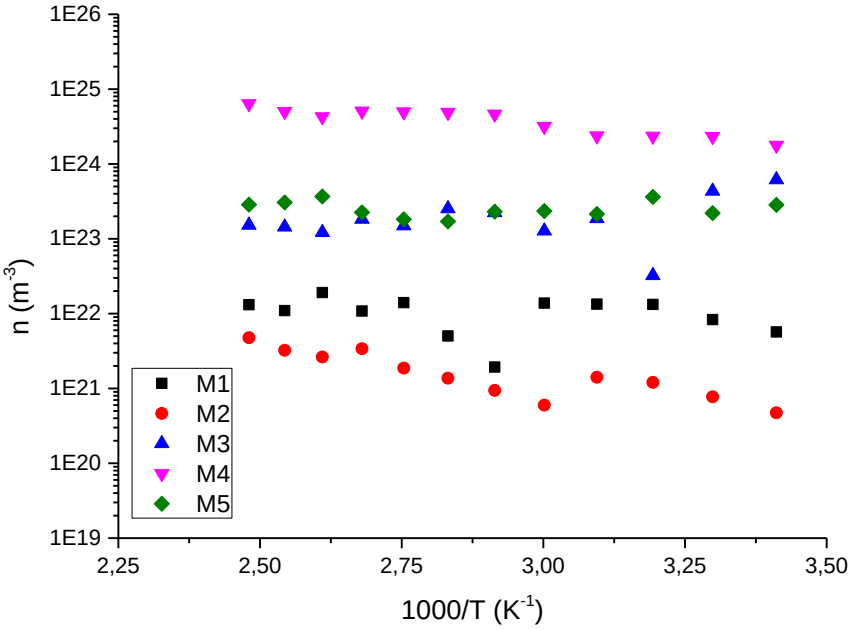

Figure 7: Variation of the anion charge density in **M1**-**M5** versus the reciprocal of temperature.

The effective Debye length associated to this kind of membranes, can play a key role to rationalize the observed behavior. The values for M obtained through the fitting of tan δ data to Eq. (5), along with the experimental data for the thicknesses of the films, have been used to calculate the Debye length from[38] $M = \frac{L}{2 \cdot L_D}$. For comparison, we also have calculated the Debye

length from $L_D = \frac{L}{2}\left(\frac{\tau}{\tau_{EP}}\right)^{1/\alpha}$, considering the values calculated for τ and τ_{EP}. The variation of the L_D values with temperature for the different films are presented in Figure 8.

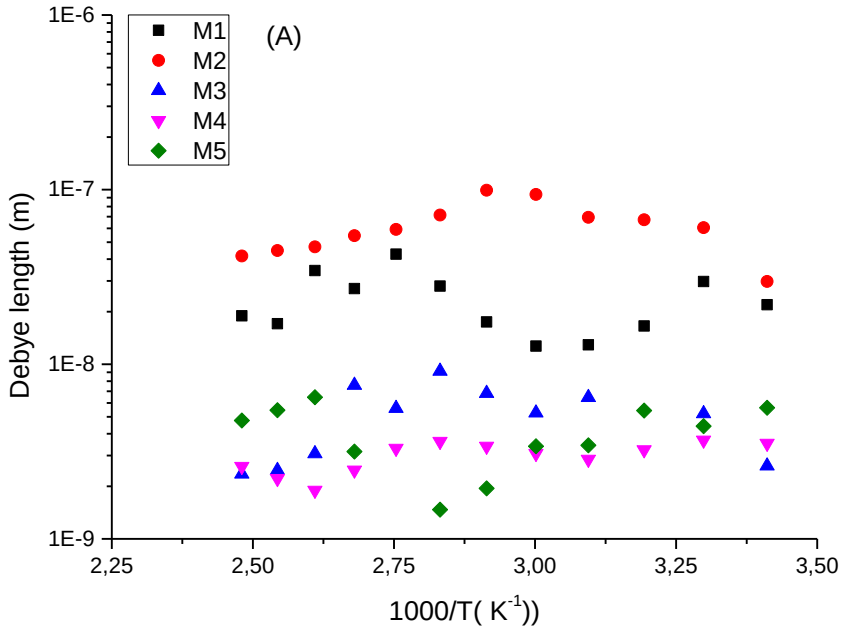

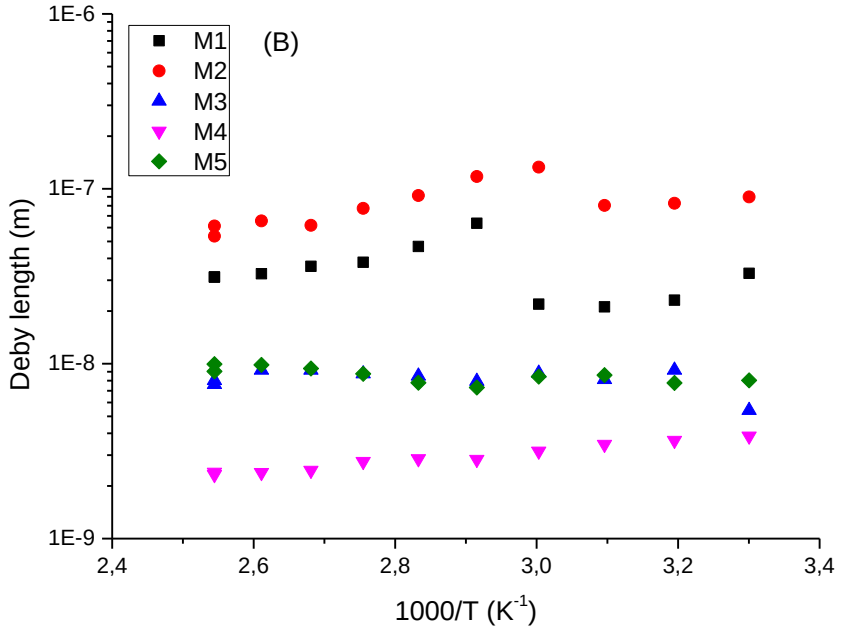

Figure 8: Variation of the Debye length with temperature for all the samples studied from: (A) from $L_D = \frac{L}{2}\left(\frac{\tau}{\tau_{EP}}\right)^{1/\alpha}$ and, (B) from $L_D = \frac{L}{2\,M}$

It must be noted that the trend for the calculated Debye length is: L_D(**M3**) < L_D(**M4**) < L_D(**M5**) < L_D(**M1**) < L_D(**M2**), being the same that one followed by the electrode polarization relaxation time, indicating that conductivity and diffusivity are in correspondence with the thickness of Debye length. Polymeric membranes **M1**-**M5** display L_D values in the range between 4-100 nm. As could be expected, the Debye layer thickness varies with the temperature reciprocally with the free charge density of the films.

Finally, when the values of the inverse Debye length can be obtained from the peaks of the loss tangent, the values of static permittivity ε_s, can be estimated from an indirect method following the Eq. (10). This method can be compared with the equation by Anatoly Serghei[53], where the permittivity can be expressed as a function of the f_{ON} and f_{Max} values found from the curves of double logarithmic plot of σ" versus frequency (see Figure SI-4 in the Supplementary Information), as stated by Serghei:

$$\varepsilon_s = \frac{\sigma_{dc}}{2\pi\varepsilon_0}\frac{f_{Max}}{f_{ON}^2} \qquad (25)$$

where f_{ON} and f_{MAX} are, respectively, the onset frequency where the electrode polarization starts to develop and the full development of electrode polarization has been built.

Figure SI-4 shows the curves of double logarithmic plot of σ" versus frequency in the whole temperature interval considered for M1, M2, M3 M4 and M5, respectively. From these figures, for each sample at each temperature, the frequency values of the onset (f_{ON}) and full development of electrode polarization (f_{MAX}) were established, respectively, which allowed the calculation of the static permittivity, such as is indicated in Eq. (25). The mean values obtained following the two procedures, (following the Cole-Cole relaxation model (Eq (10) and from Anatoli Serghei equation given in Eq. (25)) are gathered in Tables 4 and 5, respectively. Also, for comparison purposes, the values observed from the experimental plots of ε' versus frequency for all the samples were tabulated as experimental ε_s.

Table 4: Static permittivity in terms of Cole-Cole function taking into account the Eq. (10), and the experimental values ($\varepsilon_{s,exp}$) to comparison.

T (°C)	M1		M2		M3		M4		M5	
	ε_S		ε_S		ε_S		ε_S		ε_S	
	Eq(10)	Exp.	Eq(10)	Exp.	Eq(10)	Exp.	Eq(10)	Exp.	Eq(10)	Exp.
10	5.4	5.1	5.0	4,0	14.1	4.7	28.9	5.6	18.7	7.3
20	4.8	5,3	5.0	4,1	12.6	5.0	27.9	6.5	18.3	9.1
30	4.8	5,5	4.3	4,3	7.7	5.4	27.8	7.5	18.4	11.0
40	7.0	5,7	4.6	4,5	21.4	6.0	27.5	8.8	18.4	13.0
50	7.3	5,9	4.4	4,7	5.4	6.7	27.5	10.1	16.5	14.9
60	7.5	6,2	3.0	5,0	5.1	7.5	27.5	11.5	16.3	16.5
70	5.2	6,6	3.3	5,3	5.4	8.7	28.5	12.9	17.4	17.9
80	3.9	6,9	4.1	5,6	5.0	9.2	27.9	14.1	17.2	19.1
90	4.4	7,4	4.7	6,1	5.1	10.5	28.0	15.1	16.9	20.3
100	4.7	7,9	5.7	6,6	4. 9	11.1	29.6	16.0	15.7	21.6
110	5.0	8,5	5.3	7,3	7.9	13.2	29.7	16.7	16.0	23.0
120	5.3	9,3	5.6	8,0	8.9	14.7	29.3	17.6	16.4	25.3
130	5.4	10,1	6.3	8,8	8.7	15.6	29.0	18.5	15.7	26.6

Table 5: Static permittivity in terms of Cole-Cole function, taking into account the Eq. (25) from Anatoli Serghei.

T (°C)	ε_s M1	ε_s M2	ε_s M3	ε_s M4	ε_s M5
10	-	-	-	28.9	18.7
20	-	-	-	27.9	18.3
30	4.8	4.3	7.7	27.8	18.4
40	7.0	4.6	8.4	27.5	18.4
50	7.3	4.4	5.4	27.5	16.5
60	7.5	3.0	5.1	27.5	16.3
70	5.2	3.3	5.4	28.5	17.4
80	3.9	4.1	5.0	27.9	17.2
90	4.4	4.7	5.1	28.0	16.9

100	4.7	5.7	4. 9	29.6	15.7
110	5.0	5.3	7.9	29.7	16.0
120	5.3	5.6	8.9	29.3	16.4
130	5.4	6.3	8.7	29.0	15.7

A comparison between theoretical and experimental results reveals the good agreement between the static permittivity values obtained theoretically from the Cole-Cole model following Eq. (10) with respect to the experimental ones. A close inspection of these results indicates that ε_s increases when the temperature increases for all composite samples. In general, at each temperature the static permittivity follows the trend ε_s (M2) < ε_s (M1) < ε_s (M3) < ε_s (M5) < ε_s (M4). This may be related to the quantity of BMIM [NTf_2] in the SILLPs where the total amount of counteranion embedded in the polymer matrix was $n(M2)=9{,}42x10^{26}$ > $n(M1)=8{,}32x10^{26}$ > $n(M3)=7{,}0x10^{26}$ > $n(M5)=4{,}98x10^{26}$ > $n(M4)=4{,}65x10^{26}$ m^{-3}.

On the other hand, the static permittivity obtained from experimental results and calculated from the sample relaxation time, determined using the Cole-Cole model, and dc-conductivity, such as indicate in Eq. (10) shows a good agreement for the samples M1, M2 and M3 where they are not free IL embedded and practically the same amount of porogenic agent (VBIM [NTf2]) bulk IL. However, when they are free IL into the polymeric matrix the values theoretically calculated are higher than experimental ones, such as happen in case of samples M4 and M5 respectively.

Conclusions

Based on experimental measurements of conductivity, impedance, dielectric permittivity and loss tangent from electrochemical impedance spectroscopy, the ion mobility, diffusion coefficient and free charge density of BMIM [NTf_2] in Supported Ionic-Liquid-Like Phases (SILLPs)-based membranes has been determined with a reliable method based on the Cole-Cole relaxation. In addition, the Debye length of the system were calculated. The studied SILLPs show a significant increment of dc-conductivity as temperature raises. The conductivity values were obtained from Bode and Nyquist diagrams. The behavior of conductivity is

congruent in both methodologies. In the case of Nyquist diagrams the impedance of the circuit was modelled by a series combining two Cole-Cole functions.

Temperature dependence of the dc-conductivity is well described by a Vogel-Fulcher-Tamman equation, where it could also be observed an increment in conductivity with the amount of free ionic liquid, and when the amount of crosslinking agent decreases, which is associated to a higher content in polymer supported imidazolium moieties. The Vogel temperature increases for lower crosslinking degrees, and decreases with the amount of free IL in the composite.

From the values of activation energies obtained from VFT, it is suggesting that the anionic conduction in the films can occurs following two processes, the hopping between the imidazolium units, and a vehicle-type mechanism.

From an analysis based on the Eyring's absolute rates theory it was determined that the activation of entropy, and the enthalpy change both decrease with the loading of IL-like fragments for all samples. It is very interesting that the activation of entropy becomes negative for **M4** and **M5** films. It was interpreted that such values could be related with a decrease in the free volume, as the amount of free IL increases.

The Cole-Cole equation parameters were obtained by fitting the experimental loss tangent curves in order to calculate the ion mobility, diffusion coefficient and free charge density.

From the determination of the electrode polarization relaxation time and the sample relaxation time, it is suggested that the counteranion of the free IL affects the frequency at which the polarization starts to be present. The diffusion coefficients increased with temperature for all the films, which agrees with the behavior of the activation energies from the VFT fit, and of the conductivities. By other hand, the anion charge density is essentially independent of temperature and is directly related with the loading of imidazolium units in the polymer.

Debye length was calculated from the parameters of the tan δ fitting, and from relaxation times. The behavior of L_D is similar to that followed by the electrode polarization relaxation time. Beside this, there were provided several expressions stressing the relationship between all relevant quantities in this work, with de Debye length.

The results reported in this paper could contributed to a suitable determination of transport properties in electrochemical system, from dielectric spectroscopy measurements, and to relate several aspects of the characterization and behavior of the material to the Debye length in the system. Finally, a comparison between the static permittivity obtained from experimental

results and calculated from the sample relaxation time, determined using the Cole-Cole model, and dc-conductivity, such as indicate in Eq. (10) shows a good agreement for the samples M1, M2 and M3 where they are not free IL embedded and practically the same amount of porogenic agent (VBIM [NTf2]) bulk IL. However, when they are free IL into the polymeric matrix the values theoretically calculated are higher than experimental ones.

Acknowledgements

V. Compañ is grateful to Ministerio de Economia y Competitividad (MINECO), project reference: ENE/2015-69203-R. ISH acknowledges financial support by UNAM-DGAPA under grant IN117419. SIH and CGA are grateful to projects UNAM-DGAPA-PAPIIT IN114721, LANCAD-UNAM-DGTIC-276 and LANCAD-UNAM-DGTIC-385. ISH and JAPR are grateful to project UNAM-DGAPA-PAPIIT IN117419. BA and SVL are grateful to Ministerio de Ciencia Innovación to projects, RTI2018-098233-B-C22 and Pla de Promoció de la Investigación of Universitat Jaume I through project: UJI-B2019-40.

Data availability

All data that support the findings of this study are available from the corresponding author upon reasonable request.

References

[1] a) Marcus, Y. Ionic Liquid Properties: From Molten Salts to RTILs. Springer, **2018**. b) Ionic Liquid Devices. Smart Materials Series, 29. Royal Society of Chemistry, **2017**. Plechkova, N V.; Seddon, K.R. Applications of ionic liquids in the chemical industry. *Chem. Soc. Rev*. **2008**, *37*, 123–150.

[2] a) Green Sustainable Process for Chemical and Environmental Engineering and Science: Ionic Liquids as Green Solvents Earle, M.J.; Seddon, K.R. Ionic liquids. Green solvents for the future. *Pure Appl. Chem*. **2000**, *72*, 1391–1398.

[3] Dai, C.; Zhang, J.; Huang, C.; Lei, Z. Ionic liquids in selective oxidation: catalysts and solvents. *Chem. Rev*. **2017**, *117*, 6929–6983.

[4] González, L.; Escorihuela, J.; Altava, B.; Burguete, M.I.; Luis, S.V. Chiral room temperature ionic liquids as enantioselective promoters for the asymmetric aldol reaction. *Eur. J. Org. Chem*. **2014**, 5356–5363.

[5] a) ul Mustafa, M.Z.; bin Mukhtar, H.; Nordin, N.A.H.M.; Mannan, H.A.; Nasir, R.; Fazil, N. Recent Developments and Applications of Ionic Liquids in Gas Separation Membranes. *Chem. Eng. Technol.* **2019**, *42*, 2580-2593. b) Villa, R.; Alvarez, E.; Porcar, R.; Garcia-Verdugo, E.; Luis, S.V.; Lozano, P. Ionic liquids as an enabling tool to integrate reaction and separation processes, *Green Chem.* **2019**, *21*, 6527-6544. c) Rynkowska, E.; Fatyeyeva, K.; Kujawski, W. Application of polymer-based membranes containing ionic liquids in membrane separation processes: a critical review. *Rev. Chem. Eng.* **2018**, *34*, 341-363. d) Chen, D.; Ying, W.; Guo, Y.; Ying, Y.; Peng, X. Enhanced Gas Separation through Nanoconfined Ionic Liquid in Laminated MoS_2 Membrane. *ACS Appl. Mater. Interfaces* **2017**, *9*, 44251–44257.

[6] a) Wu, D.T.; Yang, J.P.; Peng, Y.G.; Yu, Y.; Zhang, J.; Guo, L.L.; Kong, Y.; Jiang, J.L. Highly enantioselective recognition of various acids using polymerized chiral ionic liquid as electrode modifiers. *Sensors Actuat. B-Chem.* **2019**, *282*, 164-170. b) González-Mendoza, L.; Escorihuela, J.; Altava, B.; Burguete, M.I.; Luis, S.V. Application of optically active chiral bis-(imidazolium) salts as potential receptors of chiral dicarboxylate salts of biological relevance. *Org. Biomol. Chem*. **2015**, *13*, 5450–5459.

[7] Valls, A.; Altava, B.; Burguete, M.I.; Escorihuela, J.; Martí-Centelles, V.; Luis, S.V. Supramolecularly assisted synthesis of chiral tripodal imidazolium compounds. *Org. Chem. Front*. **2019**, *6*, 1214–1225.

[8] González-Mendoza, L.; Altava, B.; Burguete, M.I.; Escorihuela, J.; Hernando, E.; Luis, S.V.; Quesada, R.; Vicent, C. Bis(imidazolium) salts derived from amino acids as receptors and transport agents for chloride anions. *RSC Advances* **2015**, *5*, 34415–34423.

[9] a) Moshikur, R.M.; Chowdhury, M.R.; Moniruzzaman, M.; Goto, M. Biocompatible ionic liquids and their applications in pharmaceutics. *Green Chem.* **2020**, *22*, 8116-8139. b) Marrucho, I.M.; Branco, L.C.; Rebelo L.P.N. Ionic Liquids in Pharmaceutical Applications. *Annu. Rev. Chem. Biomol. Eng*. **2014**, *5*, 527–546.

[10] Egorova, K.S.; Gordeev, E.G.; Ananikov, V.P. Biological activity of ionic liquids and their application in pharmaceutics and medicine. *Chem. Rev*. **2017**, *117*, 7132–7189.

[11] a) Karuppasamy, K.; Theerthagiri, J.; Vikraman, D.; Yim, C.J.; Hussain, S.; Sharma, R.; Maiyalagan, T.; Qin, J.Q.; Kim, H.S. Ionic Liquid-Based Electrolytes for Energy Storage Devices: A Brief Review on Their Limits and Applications. *Polymers* **2020**, *12*, 918. b) Liu, H.; Yu, H.J. Ionic liquids for electrochemical energy storage devices applications. *J. Mater. Sci. Technol.* **2019**, *35*, 674-686. c) Watanabe, M.; Thomas, M.L.; Zhang, S.; Ueno, K.; Yasuda, T.; Dokko, K. Application of ionic liquids to energy storage and conversion materials and devices. *Chem. Rev.* **2017**, *117*, 7190–7239. d) MacFarlane, D.R.; Tachikawa, N.; Forsyth, M.; Pringle, J.M.; Howlett, P.C.; Elliott, G.D.; Davis, J.H., Jr.; Watanabe, M.; Simon, P.; Angell, C.A. Energy applications of ionic liquids. *Energy Environ. Sci.* **2014**, *7*, 232–250.

[12] a) Pan, S.S.; Yao, M.; Zhang, J.H.; Li, B.S.; Xing, C.X.; Song, X.L.; Su, P.P.; Zhang, H.T. Recognition of Ionic Liquids as High-Voltage Electrolytes for Supercapacitors. *Front. Chem.* **2020**, *8*, 261. b) Shahzad, S.; Shah, A.; Kowsari, E.; Iftikhar, F.J.; Nawab, A.; Piro, B.; Akhter, M.S.; Rana, U.A.; Zou, Y.J. Ionic Liquids as Environmentally Benign Electrolytes for High-Performance Supercapacitors. *Glob. Chall.* **2019**, *3*, 1800023. c) Eftekhari, A. Supercapacitors utilising ionic liquids. *Energy Storage Mater.* **2017**, *9*, 47-69.

[13] a) Elwan, H.A.; Mamlouk, M.; Scott, K. A review of proton exchange membranes based on protic ionic liquid/polymer blends for polymer electrolyte membrane fuel cells. J. *Power Sources* **2021**, *484*, 229197. b) Ortiz, A.; Ortiz, I. Progress in the use of ionic liquids as electrolyte membranes in fuel cells. *J. Membr. Sci.* **2017**, *469*, 379–396.

[14] a) Francis, C.F.J.; Kyratzis, I.L.; Best, A.S. Lithium-Ion Battery Separators for Ionic-Liquid Electrolytes: A Review. *Adv. Mat.* **2020**, *32*, 1904205. b) Forsyth, M.; Porcarelli, L.; Wang, X.E.; Goujon, N.; Mecerreyes, D. Innovative Electrolytes Based on Ionic Liquids and Polymers for Next-Generation Solid -State Batteries. *Acc. Chem. Res.* **2019**, *52*, 686-694. c) Yang, Q.W.; Zhang, Z.Q.; Sun, X.G.; Hu, Y.S.; Xing, H.B.; Dai, S. Ionic liquids and derived materials for lithium and sodium batteries. *Chem. Soc. Rev.* **2018**, *47*, 2020-2064. d) Song, X.; Ding, L.; Wang, L.; He, M.; Han; X. Polybenzimidazole membranes embedded with ionic liquids for use in high proton selectivity vanadium redox flow batteries. *Electrochim, Acta* **2019**, *295*, 1034−1043.

[15] Fehrmann, R.; Riisager, A.; Haumann, M; Eds. Supported Ionic Liquids. Fundamentals and Applications. Wiley-VCH, **2014**.

[16] Montolio, S.; Altava, B.; Garcia-Verdugo, E.; et ál. Supported ILs and Materials Based on ILs for the Development of Green Synthetic Processes and Procedures, in Green Synthetic Processes and Procedures, Ballini, R., Ed.; RSC Green Chemistry Series, 61, pp. 289-318, **2019**.

[17] a) Eftelchari, A.; Saito, T. Synthesis and properties of polymerized ionic liquids. *Eur. Polym. J.* **2017**, *90*, 245-272. b) Qian, W.J.; Texter, J.; Yan, F. Frontiers in poly(ionic liquid)s: syntheses and applications. *Chem. Soc. Rev.*, **2017**, *46*, 1124-1159. c) Inoue, T.; Matsumoto, A.; Nakamura, K. Dynamic Viscoelasticity and Birefringence of Poly(ionic liquids) in the Vicinity of Glass Transition Zone. *Macromolecules* **2013**, *46*, 6104-6109. d) Nakamura, K.; Fukao, K. Dielectric relaxation behavior of polymerized ionic liquids with various charge densities. *Polymer* **2013**, *54*, 3306-3313. e) Nakamura, K.; Fukao, K.; Inoue, T. Dielectric Relaxation and Viscoelastic Behavior of Polymerized Ionic Liquids with Various Counteranions. *Macromolecules* **2012**, *45*, 3850-3858.

[18] a) Mecerreyes, D. Applications of Ionic Liquids in Polymer Science and Technology. Springer. **2016**. b) Mecerreyes, D. Poly(ionic liquid)s: An update *Prog. Polym Sci.* **2013**, 38, 1009-1036. c) Mecerreyes, D. Polymeric ionic liquids: Broadening the properties and applications of polyelectrolytes. *Prog. Polym Sci.* **2011**, 36, 1629-1648.

[19] Ye, Y.-S.; Ricka, J.; Hwang, B.-J. Ionic liquid polymer electrolytes. *J. Mater. Chem. A* **2013**, *1*, 2719–2743.

[20] Lee, C.P.; Ho, K.C. Poly(ionic liquid)s for dye-sensitized solar cells: A mini-review. *Eur. Polym. J.* **2018**, *108*, 420-428.

[21] Garcia-Bernabé, A.; Rivera, A.; Granados, A.; Luis, S.V.; Compañ, V. *Electrochim. Acta* **2016**, *213*, 887.

[22] a) Sans, V.; Karbass, N.; Burguete, M.I.; Compañ, V.; Garcia-Verdugo, E.; Luis, S.V.; Pawlak M. *Chem. Eur. J.* **2011**, *17*, 1894-1096. b) Garcia-Bernabé, A.; Compañ, V.; Burguete, M.I.; Garcia-Verdugo, E.; Karbass, N.; Luis, S.V.; Riande, E. *J. Phys. Chem. C* **2010**, *114*, 7030-7037. c) Compañ, V.; Molla, S.; Garcia-Verdugo, E.; Luis, S.V.; Burguete, M.I. *J. Non-Cryst. Solids* **2012**, *358*, 1228-1237.

[23] Altava, B.; Compañ, V.; Andrio, A.; del Castillo, L.F.; Mollá, S.; Burguete, M.I.; Garcia-Verdugo, E.; Luis, S.V. *Polymer* **2015**, *72*, 69-81.

[24] Valverde, D.; Garcia-Bernabé, A.; Andrio, A.; Garcia-Verdugo, E.; Luis, S.V.; Compañ, V. *Phys. Chem. Chem. Phys.* **2019**, *21*, 17923-17932.

[25] Andrio, A.; Hernández, S.I.; García-Alcantara, C.; del Castillo, L.F.; Compañ, V.; Santamaria-Holek, I. Temperature dependence of anomalous protonic and superprotonic transport properties in mixed salts based on CsH_2PO_4 *Phys. Chem. Chem. Phys.* **2019**, *21*, 12948-12960.

[26] a) Bakonyi, P.; Kook, L .; Rozsenberszki, T.; Toth, G.; Belafi-Bako, K.; Nemestothy, N. Development and Application of Supported Ionic Liquid Membranes in Microbial Fuel Cell Technology: A Concise Overview. *Membranes* **2020**, *10*, 16. b) Liu, F.X.; Wang, S.; Li, J.S., Tian X., Wang, X.; Chen, H.; Wang, Z. Polybenzimidazole/ionic-liquid-functional silica composite membranes with improved proton conductivity for high temperature proton exchange membrane fuel cells. *J. Membr. Sci.* **2017**, *541*, 492-499. c) Liu, S.; Zhou, L.; Wang, P.; Zhang, F.; Yu, S.; Shao, Z.; Yi, B. Ionic-Liquid-Based Proton Conducting Membranes for Anhydrous H_2/Cl_2 Fuel-Cell Applications. *ACS Appl. Mater. Interfaces* **2014**, *6*, 3195−3200. d) Rana, U.A.; Forsyth, M.; MacFarlane, D.R.; Pringle, J.M. Toward protic ionic liquid and organic ionic plastic crystal electrolytes for fuel cells. *Electrochim. Acta* **2012**, *84*, 213-222.

[27] Wang, J. T-W.; Hsu, S. L.-C. Enhanced high-temperature polymer electrolyte membrane for fuel cells based on polybenzimidazole and ionic liquids. *Electrochim. Acta* **2011**, *56*, 2842–2846.

[28] van de Ven, E.; Chairuna, A.; Merle, G.; Pacheco Benito, S.; Borneman, S.; Nijmeijer, K. Ionic liquid doped polybenzimidazole membranes for high temperature Proton Exchange Membrane fuel cell applications. *J. Power Sources* **2013**, *222*, 202–209.

[29] a) Shütt, H.J. Determination of the free ionic carrier concentration – A discussion of different methods. *Solid State Ionics* **1994**, *70*, 505-510. (b) Shütt, H.J.; Gerdes, E. Space-charge relaxation in ironically conducting oxide glasses. 1. Model and frequency-response. *J. Non-Cryst. Solids.* **1992**, *144*, 1-13.

[30] Coelho, R. Physics of Dielectrics, Elsevier Scientific Publishing Company, NY, **1979**, pp. 97-102.

[31] Jönsson, M.; Welch, K.; Hamp, S.; Stromme, M. Bacteria counting with impedance spectroscopy in a micro probe station *J. Phys. Chem. B*, **2006**, *110*, 10165-10169.

[32] Trukhan, E.M. Dispersion of the dielectric constant of heterogeneous systems. *Sov. Phys. Solid State* 1963, *4*, 2560-2570.

[33] Sorensen, T.S.; Compañ, V.; Diaz-Calleja, R. Complex permittivity of a film of poly [4-(acryloxy)phenyl(4-chlorophenyl)methanone] containing free ion impurities and the separation of the contributions from interfacial polarization, Maxwell-Wagner-Sillars effects and dielectric relaxations of the polymer chains. *J. Chem. Soc. Faraday Trans.* **1996**, *91*, 4235-4250.

[34] MacDonald, J.R. Theory of AC space-charge polarization effects in photoconductors, semiconductors, and electrolytes. *Phys. Rev.* **1953**, *92*, 4-17.

[35] MacDonald, J.R. Simplified impedance/frequency-response results for intrinsically conducting solids and liquids. *J. Chem. Phys.* **1974**, *61*, 3977-3996.

[36] Coelho, R. On the static permittivity of dipolar and conductive media – An educational approach. *J. Non-Cryst. Solids* **1991**, *131*, 1136-1139.

[37] Coelho, R. On the relaxation of a space-charge. *Rev. Phys. Appl.* **1983**, *18*, 137-146.

[38] Klein, R.J.; Zhang, S.H.; Dou, S.; Jones, B.H.; Colby, R.H.; Runt, J. Modeling electrode polarization in dielectric spectroscopy: Ion mobility and mobile ion concentration of single-ion polymer electrolytes. *J. Chem. Phys.* **2006**, *124*, 144903.

[39] Tang, J.B.; Tang, H.D.; Sun, W.L.; Plancher, H.; Radosz, M.; Shen, Y.Q. Poly(ionic liquid)s: a new material with enhanced and fast CO_2 absorption. *Chem. Commun.* **2009**, *26*, 3325-3327.

[40] Huddleston, J.G.; Visser, A.E.; Reichert, W.M.; Willauer, H.D.; Broker, G.A.; Rogers, R.D. Characterization and comparison of hydrophilic and hydrophobic room temperature ionic liquids incorporating the imidazolium cation. *Green Chem.* **2001**, *3*, 156-164.

[41] Randviir, E.P.; Banks, C.E. Electrochemical impedance spectroscopy: an overview of bioanalytical applications. *Anal. Methods* **2013**, *5*, 1098–1115.

[42] Compañ, V.; Escorihuela, J.; Olvera, J.; García-Bernabé, A., Andrio, A. Influence of the anion on diffusivity and mobility of ionic liquids composite polybenzimidazole membranes. *Electrochim. Acta* **2020**, *354*, 136666.

[43] Maxwell, J.C. A Treatise on Electricity and Magnetism. Chapters I-IV, reprinted in Cambridge University Press, Cambridge, **2010**.

[44] Sillars, R.W. The properties of a dielectric containing semiconducting particles of various shapes *J. Proc. Inst. Electr. Eng.* **1937**, *80*, 378-394.

[45] Fuentes, I.; Andrio, A.; Garcia-Bernabé, A.; Escorihuela, J.; Vinas, C.; Teixidor, F.; Compan, V. Structural and dielectric properties of cobaltacarborane composite polybenzimidazole membranes as solid polymer electrolytes at high temperature. *Phys. Chem. Chem. Phys.* **2018**, *20*, 10173-10184.

[46] Bode, H.W. *Network Analysis and Feedback Amplifier Design*; Van Nostrand: Princeton, NJ, USA, **1945**.

[47] Nyquist, H. Thermal agitation of electric charge in conductors. *Phys. Rev.* **1928**, *32*, 110-113.

[48] Orazem, M. E.; Tribollet, B. Electrochemical Impedance Spectroscopy, 2nd ed., John Wiley & Sons, Inc., Hoboken, New Jersey 2017.

[49] Escorihuela, J.; Narducci, R.; Compañ, V.; Costantino, F. Proton conductivity of composite polyelectrolyte membranes with metal-organic frameworks for fuel cell applications. *Adv. Mater. Interfaces* **2019**, 6, 1801146.

[50] Vega-Moreno, J.; Lemus-Santana, A.A.; Reguera, E.; Andrio, A.; Compañ, V. High proton conductivity at low and moderate temperature in a simple family of Prussian blue analogs, divalent transition metal hexacyanocobaltates (III). *Electrochim. Acta* **2020**, 360, 136959.

[51] Huber, B.; Rossrucker, L.; Sundermeyer, J.; Roling, B. Ion transport properties of ionic liquid-based polyelectrolytes. *Solid State Ionics*, **2013**, *247-248*, 15-21.

[52] Wang, Y.; Sun, C.N.; Fan, F.; Sangoro, J.R.; Berman, M.B.; Greenbaum, S.G.; Zawodzinski, T.A.; Sokolov, A.P. Examination of methods to determine free-ion diffusivity and number density from analysis of electrode polarization. *Phys Rev. E* **2013**, *87*, 042308.

[53] Serghei A.; Tress M.: Sangoro J. R; Kremer F. Electrode polarization and charge transport at solid interfaces. *Phys Rev. E* **2009**, *80*, 184301.

Supplementary Information

Debye length and anionic transport properties on composite membranes based on Supported Ionic Liquid-Like Phases (SILLPs)

Saúl. I. Hernández,[+] Belen Altava,[±] J. A. Portillo-Rodriguez,[++] Iván Santamaría-Holek,[+] C.García-Alcántara,[+] Santiago V. Luis[±] , Vicente Compañ[•,*]

[+] Unidad Multidisciplinaria de Docencia e Investigación-Juriquilla, Facultad de Ciencias, Universidad Nacional Autónoma de México (UNAM), Juriquilla, Querétaro, CP 76230, México

[±] Departamento de Química Orgánica, Universitat Jaume I, 12080-Castellón de la Plana, Spain

[•,*] Departamento de Termodinámica Aplicada, Universitat Politècnica de Valencia, C/Camino de Vera s/n, 46022-Valencia, Spain

Author correspondence: Vicente Compañ, E-mail: vicommo@ter.upv.es

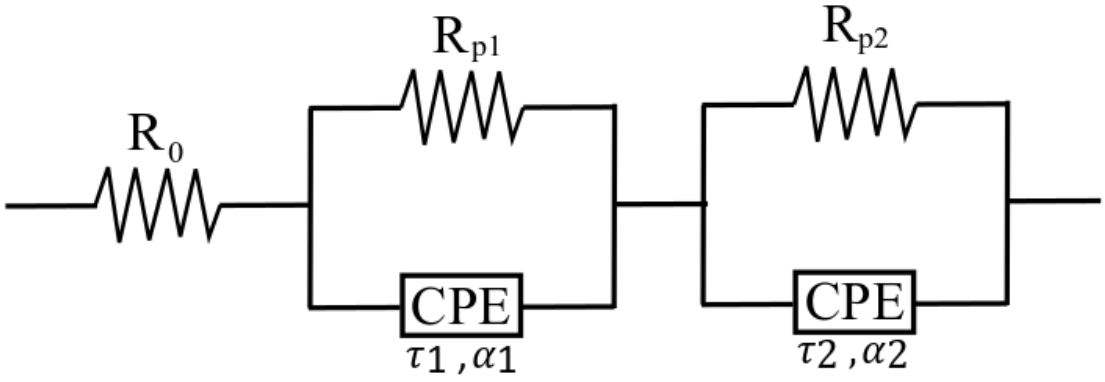

Figure SI-1: Equivalent circuit that comprises a resistance R_{pi} representing the charge transfer resistance at the interface sample/electrode in parallel with a constant phase element (CPE), representing the sample/electrode double layer.

Table SI-1: Values of the different parameters obtained from the fitting of the Nyquist plot experimental data for the real and imaginary impedance of the films using the Eq. (1) at different temperatures.

M1							
$T\ [°C]$	$R_{p,1}\ [\Omega]$	α_1	$\tau_1\ [s]$	$R_{p,2}\ [\Omega]$	α_2	$\tau_2\ [s]$	$R_0\ [\Omega]$
30	1.45E+07	7.78E-01	5.79E-04	5.68E+07	4.66E-01	3.54E+00	5.50E-10
70	1.20E+05	7.35E-01	5.05E-06	7.27E+08	5.09E-01	1.53E+05	5.50E-10
90	1.60E+09	5.88E-01	9.72E+05	2.49E+04	7.09E-01	1.53E-06	5.50E-10
110	4.80E+03	7.75E-01	1.95E-07	4.00E+05	4.51E-01	8.00E+00	0.00E+00
120	2.70E+03	7.75E-01	9.96E-08	3.00E+05	4.51E-01	8.00E+00	0.00E+00
M2							
$T\ [°C]$	$R_{p,1}\ [\Omega]$	α_1	$\tau_1\ [s]$	$R_{p,2}\ [\Omega]$	α_2	$\tau_2\ [s]$	$R_0\ [\Omega]$
30	8.02E+06	7.30E-01	2.66E-04	2.56E+08	6.20E-01	2.05E+01	7.53E-10
70	3.96E+04	7.98E-01	5.99E-06	1.99E+08	4.94E-01	9.57E+04	0.00E+00
90	6.76E+03	7.98E-01	5.99E-07	7.59E+07	4.84E-01	9.57E+04	0.00E+00
110	5.06E+05	5.52E-01	5.15E+00	1.73E+03	7.77E-01	1.86E-07	0.00E+00
120	8.79E+04	5.52E-01	1.45E+00	9.56E+02	7.97E-01	1.96E-07	0.00E+00
M3							
$T\ [°C]$	$R_{p,1}\ [\Omega]$	α_1	$\tau_1\ [s]$	$R_{p,2}\ [\Omega]$	α_2	$\tau_2\ [s]$	$R_0\ [\Omega]$
30	8.01E+05	8.54E-01	2.37E-05	2.79E+09	4.84E-01	2.09E+07	0.00E+00
70	7.76E+03	8.38E-01	2.25E-07	1.85E+09	5.58E-01	2.58E+07	0.00E+00
90	1.86E+03	8.38E-01	5.46E-08	1.85E+09	5.58E-01	2.58E+07	0.00E+00
110	6.42E+02	8.22E-01	1.88E-08	6.51E+08	5.83E-01	1.10E+07	0.00E+00
120	4.10E+02	8.22E-01	1.48E-08	6.51E+08	5.83E-01	1.10E+07	0.00E+00
M4							
$T\ [°C]$	$R_{p,1}\ [\Omega]$	α_1	$\tau_1\ [s]$	$R_{p,2}\ [\Omega]$	α_2	$\tau_2\ [s]$	$R_0\ [\Omega]$
30	5.95E+03	7.84E-01	2.94E-07	1.65E+04	8.72E-01	6.40E-02	0.00E+00
70	3.10E+02	9.00E-01	2.07E-08	3.07E+04	8.32E-01	9.00E-02	6.50E+01
90	9.00E+01	9.90E-01	1.27E-08	2.57E+04	8.32E-01	9.00E-02	6.50E+01

110	3.70E+01	9.90E-01	9.81E-09	4.50E+09	8.00E-01	9.04E+05	4.00E+01
120	1.64E+01	9.90E-01	8.81E-09	4.50E+09	8.00E-01	9.04E+05	4.00E+01
M5							
$T\ [°C]$	$R_{p,1}\ [\Omega]$	α_1	$\tau_1\ [s]$	$R_{p,2}\ [\Omega]$	α_2	$\tau_2\ [s]$	$R_0\ [\Omega]$
30	2.98E+02	7.40E-01	3.24E-08	3.95E+04	8.50E-01	9.97E-02	0.00E+00
70	3.62E+01	8.00E-01	3.34E-09	2.05E+04	8.40E-01	9.97E-02	0.00E+00
90	1.78E+01	8.60E-01	2.00E-09	2.05E+04	8.53E-01	9.97E-02	0.00E+00
110	9.78E+00	9.50E-01	1.54E-09	1.55E+04	8.53E-01	9.97E-02	0.00E+00
120	7.60E+00	9.90E-01	1.54E-09	1.15E+04	8.53E-01	9.97E-02	0.00E+00

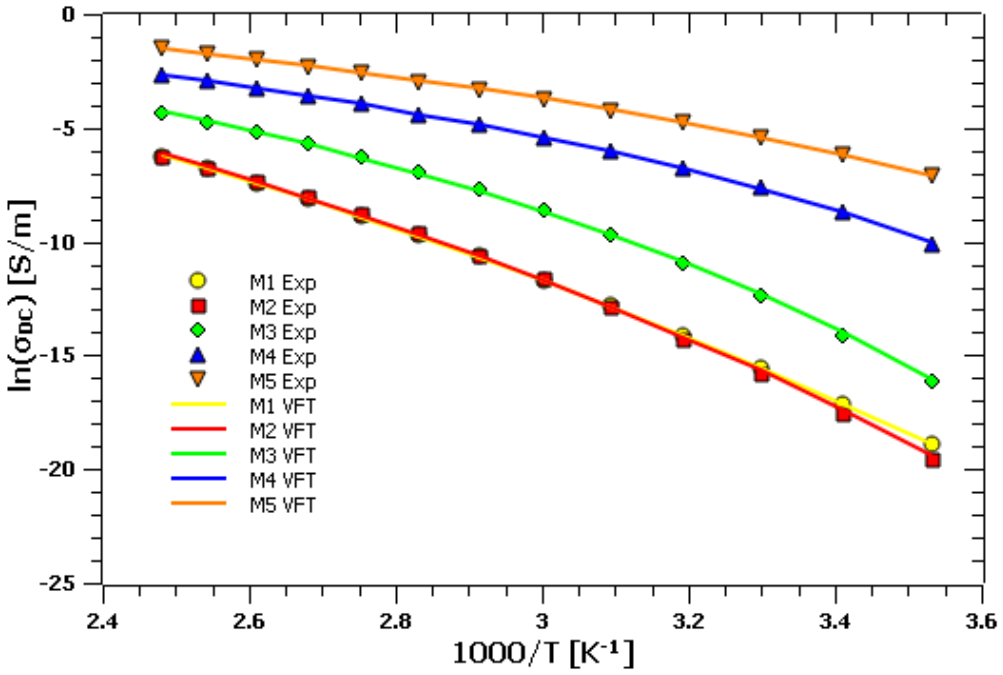

Figure SI-2: Temperature dependence of conductivity for the different samples studied. The lines represent the fit of experimental data following the VFT equation (Eq. (3) in the main text).

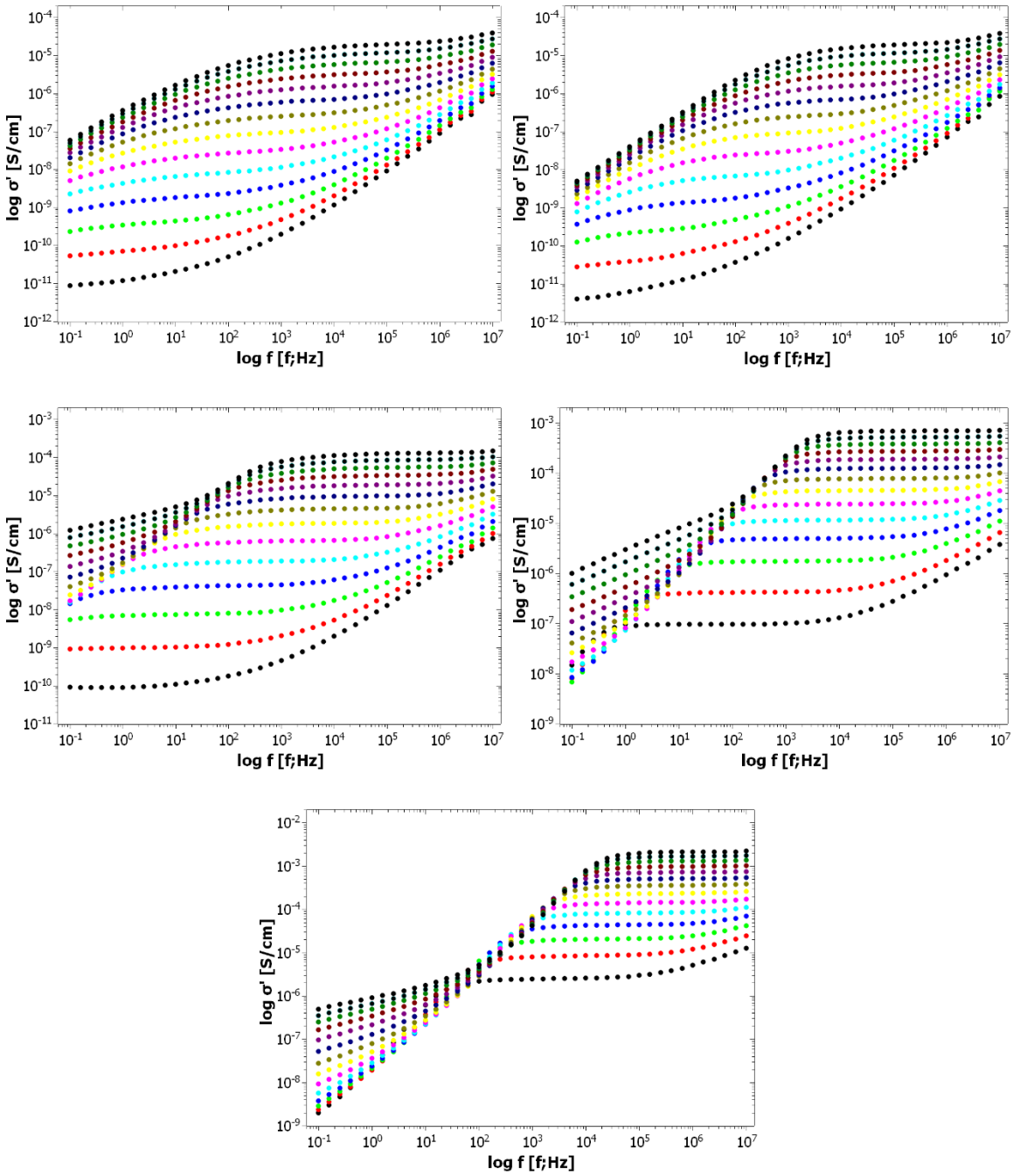

Figure SI-3: Log σ' versus log f for all the membranes (M1-M5) in all the range of temperatures (● 0°C, ● 10°C, ● 20°C, ● 30°C, ● 40°C, ● 50°C, ● 60°C, ● 70°C, ● 80°C, ● 90°C, ● 100°C, ● 110°C, ● 120°C, ● 130°C).

Table SI-2: Calculated values for M, τ_{EP} and α using Eq. (5) in the main text, for the temperatures 20, 40, 40, 80, 100 and 120 ºC.

	T = 20°C			T = 40°C		
Membrane	**M**	**τ_{EP} (s)**	**α**	**M**	**τ_{EP} (s)**	**α**
M1	2.33E+03	9.74E+00	8.90E-01	3.15E+03	6.98E-01	8.95E-01
M2	9.82E+02	5.65E+00	8.72E-01	9.07E+02	2.05E-01	8.92E-01
M3	1.89E+04	3.12E+00	9.72E-01	1.86E+03	2.20E-01	8.28E-01
M4	1.76E+04	2.67E-02	9.93E-01	2.06E+04	3.98E-03	9.93E-01
M5	8.83E+03	8.29E-04	9.82E-01	9.66E+03	2.07E-04	9.85E-01
	T = 60°C			**T = 80°C**		
Membrane	**M**	**τ_{EP} (s)**	**α**	**M**	**τ_{EP} (s)**	**α**
M1	3.72E+03	6.43E-02	9.05E-01	1.60E+03	4.41E-03	9.30E-01
M2	5.64E+02	9.48E-03	9.22E-01	8.20E+02	1.73E-03	9.23E-01
M3	8.49E+03	5.25E-03	9.80E-01	8.82E+03	9.97E-04	9.81E-01
M4	2.37E+04	1.02E-03	9.94E-01	2.62E+04	3.75E-04	9.94E-01
M5	8.89E+03	6.54E-05	9.88E-01	9.63E+03	3.11E-05	9.91E-01
	T = 100°C			**T = 120°C**		
Membrane	**M**	**τ_{EP} (s)**	**α**	**M**	**τ_{EP} (s)**	**α**
M1	2.08E+03	1.11E-03	9.34E-01	2.39E+03	3.48E-04	9.39E-01
M2	1.21E+03	5.01E-04	9.25E-01	1.22E+03	1.39E-04	9.38E-01
M3	8.16E+03	2.76E-04	9.80E-01	9.35E+03	1.97E-04	9.78E-01
M4	3.05E+04	1.81E-04	9.94E-01	3.13E+04	9.42E-05	9.94E-01
M5	7.99E+03	1.48E-05	9.95E-01	7.25E+03	9.01E-06	9.97E-01

Figure SI-4 shows the curves of double logarithmic plot of σ" versus frequency in the whole temperature interval considered for M1, M2, M3 M4 and M5, respectively. From this figure, for each sample at each temperature, the frequency values of the onset (f_{ON}) and full development of electrode polarization (f_{MAX}) were established, respectively, which allowed the calculation of the static permittivity, such as is indicate following Eq. (25). The mean values obtained following the two procedures are gathered in **Table 5** as theoretical ε_s. Also, for comparison purposes, the values observed from the experimental plots of ε' versus frequency for all the samples were tabulated as experimental ε_s. A comparison between theoretical and experimental results reveals the excellent agreement between the static permittivity values obtained theoretically following Eq. (9) with respect to the experimental ones. A close inspection of these results indicates that ε_s decreases when the temperature increases for the M1, M2, M3, M4 and M5, composite samples.

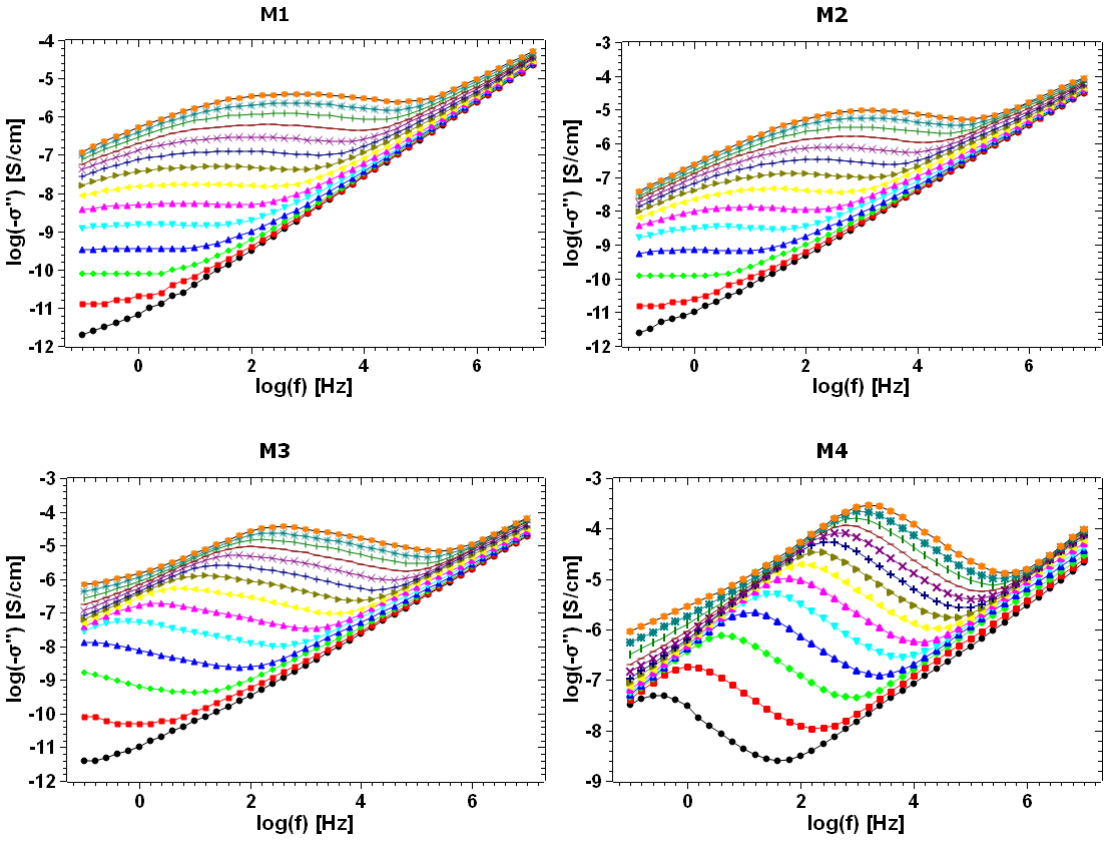

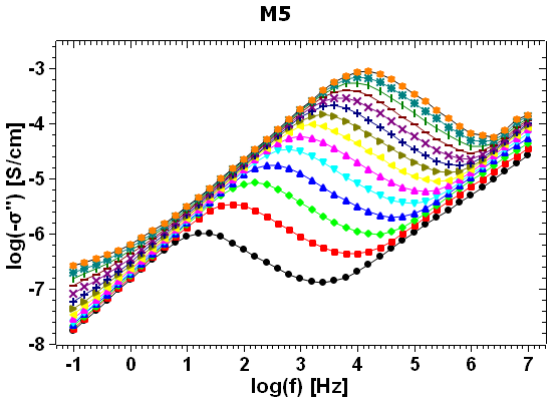

Figure SI-4: Double logarithmic plot of σ" versus frequency in all the range of temperatures (● 0°C, ■ 10°C, ♦ 20°C, ▲ 30°C, ▼ 40°C, ▲ 50°C, ◄ 60°C, ► 70°C, + 80°C, x 90°C, - 100°C, | 110°C, ⁎ 120°C, ⁎ 130°C). The values of the f_{ON} and f_{MAX} are determined from this curves and used in the Serghei expression Eq. (25) in the main text.

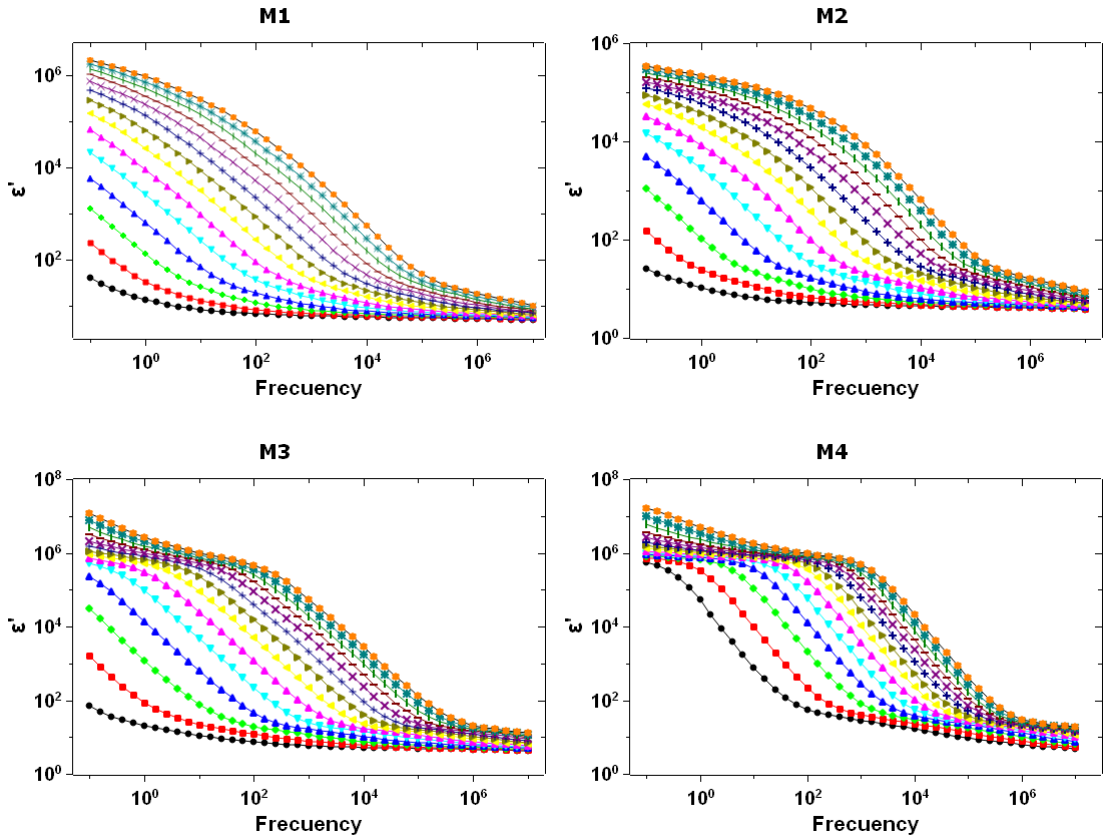

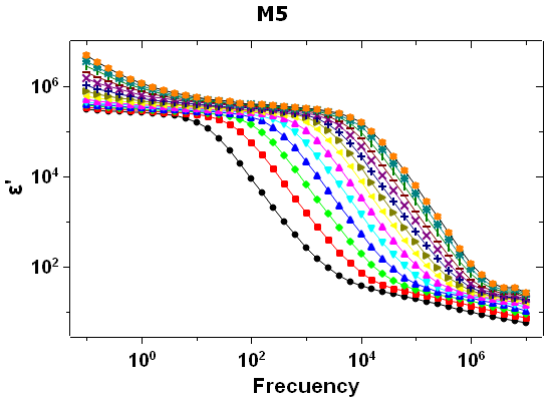

Figure SI-5: Double logarithmic plot of ε' versus frequency for all the studied samples in all the range of temperatures (● 0°C, ■ 10°C, ♦ 20°C, ▲ 30°C, ▼ 40°C, ▲ 50°C, ◄ 60°C, ► 70°C, + 80°C, **x** 90°C, - 100°C, | 110°C, * 120°C, * 130°C).

Table SI-3: Static permittivity in terms of Cole-Cole function, taking into account the Eq.(9) and the experimental values ($\varepsilon_{s,exp}$), to comparison.

T (°C)	M1		M2		M3		M4		M5	
	ε_S		ε_S		ε_S		ε_S		ε_S	
	Eq(9)	Exp.	Eq(9)	Exp.	Eq(9)	Exp.	Eq(9)	Exp.	Eq(9)	Exp.
10	5.4		5.0		14.1	16.4	28.9	27.5	18.7	2.9
20	4.8		5.0		12.6	17.7	27.9	29.8	18.3	23.8
30	4.8		4.3		7.7	13.6	27.8	12.4	18.4	23.2
40	7.0		4.6	24.1	21.4	7.6	27.5	22.3	18.4	19.6
50	7.3	32.9	4.4	17.8	5.4	1.3	27.5	13.1	16.5	9.3
60	7.5	19.1	3.0	18.1	5.1	1.8	27.5	10.8	16.3	10.2
70	5.2	24.0	3.3	10.0	5.4	1.3	28.5	12.8	17.4	10.4
80	3.9	11.3	4.1	11.4	5.0	1.3	27.9	13.9	17.2	10.0
90	4.4	11.4	4.7	11.8	5.1	1.7	28.0	14.1	16.9	9.2
100	4.7	16.3	5.7	7.0	4. 9	1.3	29.6	13.5	15.7	12.9
110	5.0	13.8	5.3	14.4	7.9	1.5	29.7	12.3	16.0	11.1
120	5.3	17.0	5.6	7.1	8.9	1.5	29.3	10.8	16.4	23.5

130	5.4	7.9	6.3	5.1	8.7	1.5	29.0	14.7	15.7	10.5

Table SI-4: Static permittivity in terms of Cole-Cole function, taking into account the Eq.(9) and calculated from Eq. (25)

T (°C)	M1		M2		M3		M4		M5	
	ε_S		ε_S		ε_S		ε_S		ε_S	
	Eq(9)	Exp	Eq(9)	Exp	Eq(9)	Exp	Eq(9)	Exp	Eq(9)	Exp
10	5.4	5.4	5.0	4.3	14.1	4.9	28.9	7.8	18.7	13.9
20	4.8	5.7	5.0	4.5	12.6	5.3	27.9	10.2	18.3	17.5
30	4.8	6.0	4.3	4.7	7.7	5.8	27.8	12.7	18.4	20.4
40	7.0	6.3	4.6	5.0	21.4	6.5	27.5	15.2	18.4	22.5
50	7.3	6.8	4.4	5.5	5.4	7.5	27.5	17.3	16.5	24.6
60	7.5	7.3	3.0	6.0	5.1	8.9	27.5	18.8	16.3	27.0
70	5.2	8.0	3.3	6.8	5.4	10.4	28.5	19.9	17.4	30.6
80	3.9	8.9	4.1	7.8	5.0	12.1	27.9	20.9	17.2	35.3
90	4.4	10.2	4.7	9.1	5.1	13.6	28.0	21.7	16.9	42.5
100	4.7	11.8	5.7	10.9	4. 9	14.9	29.6	23.1	15.7	53.2
110	5.0	13.7	5.3	12.7	7.9	16.3	29.7	24.8	16.0	69.8
120	5.3	16.0	5.6	14.6	8.9	18.2	29.3	26.6	16.4	91.2
130	5.4	18.6	6.3	16.0	8.7	20.7	29.0	29.3	15.7	120.0